JOHANNES GUTENBERG UNIVERSITÄT MAINZ

JG|U

Automated Positioning Control for Trapped-Ion Quantum Registers

von

Janine Nicodemus

Masterarbeit in Physik
vorgelegt dem Fachbereich Physik, Mathematik und Informatik (FB 08)
der Johannes Gutenberg-Universität Mainz
am 19. Oktober 2017

1. Gutachter: Prof. Dr. Ferdinand Schmidt-Kaler
2. Gutachter: Prof. Dr. Patrick Windpassinger

Ich versichere, dass ich die Arbeit selbstständig verfasst und keine anderen als die angegebenen Quellen und Hilfsmittel benutzt sowie Zitate kenntlich gemacht habe.

Mainz, den 19.10.2017

Janine Nicodemus
QUANTUM
Institut für Physik
Staudingerweg 7
Johannes Gutenberg-Universität D-55099 Mainz
jnicodem@students.uni-mainz.de

Abstract

Trapped ions in a segmented Paul trap are a very promising candidate to implement a scalable quantum logic processor. To address individual ions and to perform two-qubit entanglement gates between specific ions we perform shuttling operations, such as movement of ions between memory and laser interaction zones, ion crystal separation and rearrangement of ions in linear strings. To perform multiple high fidelity quantum gates, these shuttling operations have to be carried out on short time scales (e.g. $< 30\,\mu$s) and with minimal induced motional excitation.
In this thesis, two advances towards fast ion shuttling and high fidelity quantum gates are presented. First, the "Segmented Ion Trap CONtrol System" (SITCONS) software framework, which allows for an automated generation of optimized voltage waveforms for multi-qubit register shuttling, is introduced. During this work, the first version of the framework was completed and integrated in the experimental control software. The tool was successfully used to generate and test voltage ramps, to accomplish ion crystal separation and ion crystal transport along the trap axis. Automatically generated transport over multiple segments with low motional excitations was successfully demonstrated.
The second goal of this work was to reduce the magnetic field fluctuations in the ion trap, in order to reduce the decoherence of our magnetic field sensitive $^{40}Ca^{+}$ spin qubit, which in turn allows for higher quantum gate fidelities.
To characterize the existing permanent magnet setup, a temperature sensor with a resolution of 0.01 °C was installed. In combination with these temperature measurements, a characterization of the long-term drifts of the qubit frequency was carried out. Comparisons of these measurements showed an almost perfect correlation between the reversible temperature drift of the permanent magnets and the frequency drift.
Therefore, a second-generation permanent magnet setup was developed with the aim to significantly improve the stability of the quantizing magnetic field by reducing the effects of temperature drifts on the permanent magnets. Two counteracting permanent magnets, namely magnets made of Sm_2Co_{17} and NdFeB, were utilized, to passively compensate the temperature induced drift of the magnetic field magnitude at the trapped ion location. As a result, the dependence of the magnetic field drift on the temperature could be reduced by about 60 %. Additionally, the overall temperature drift was substantially reduced via technical measures. In total, a tenfold reduction of the total qubit frequency drift in a long-term measurement (> 8 h) was achieved, which will be of significant importance for upcoming experiments with multiple high fidelity quantum operations.
Randomized benchmarking was performed with the previous and improved permanent magnet setup to allow for a direct comparison and showed that mean single qubit gate fidelities after idle times could be significantly increased. For instance, the mean single qubit gate fidelity for 10 logic gate operations, with an idle time of 0.4 ms after each gate, could be increased from 97.3 % to 99.1 %.

Zusammenfassung

Automatisierte Positionskontrolle für Quantenregister aus gefangenen Ionen

Eine vielversprechende Möglichkeit zur Realisierung eines skalierbaren Quantenprozessors sind gefangene Ionen in einer segmentierten Paul Falle. Um einzelne Ionen anzusprechen und Zwei-Qubit-Verschränkungsoperationen zwischen spezifischen Ionen durchzuführen, sind verschiedene Bewegungsoperationen nötig: Transport von Ionen zwischen Speicher- und Laserinteraktionszonen, die Ionenkristalltrennung und der Positionstausch von Ionen in einer linearen Anordnung. Um mehrere Quantengatter mit hoher Güte durchzuführen, müssen diese Verschiebeoperationen auf kurzen Zeitskalen (z.B. $< 30\,\mu$s) und mit minimal induzierter Anregung der Bewegungsmoden durchgeführt werden.
In dieser Arbeit werden zwei Fortschritte in Richtung schneller Ionen-Verschiebeoperationen und Quantengatter mit hoher Güte vorgestellt. Zunächst wird das Software-Framework "Segmented Ion Trap CONtrol System" (SITCONS) vorgestellt, das eine automatisierte Erzeugung von optimierten Spannungskonfigurationen für Multi-Qubit-Register Verschiebeoperationen ermöglicht. Während dieser Arbeit wurde die erste Version des Frameworks fertiggestellt und in die experimentelle Steuerungssoftware integriert. SITCONS wurde erfolgreich verwendet, um Spannungsrampen für Ionenkristalltrennungen und Ionentransporte entlang der Fallenachse zu generieren. Der automatisch erzeugte Transport über mehrere Segmente wurde experimentell erfolgreich durchgeführt und eine ausreichend niedrige Anregung des Bewegungszustandes bei deutlich verkürzten Operationszeiten erreicht.
Das zweite Ziel dieser Arbeit war es, die Magnetfeldfluktuationen in der Ionenfalle zu reduzieren, um somit die Dephasierung und damit die Dekohärenz unseres magnetfeldsensitiven $^{40}Ca^{+}$ Spin Qubits zu reduzieren und die Güte der Gatteroperationen zu erhöhen.
Zur Charakterisierung des bestehenden Permanentmagnetaufbaus wurde ein Temperatursensor mit einer Auflösung von $0.01\,^{\circ}$C integriert. In Kombination mit diesen Temperaturmessungen war eine Charakterisierung der Langzeitdrifts der Qubit-Frequenz möglich. Ein Vergleich zeigte eine starke Korrelation zwischen dem reversiblen Temperaturdrift der Permanentmagnete und dem Frequenzdrift.
Daher wurde ein neuer Permanentmagnetaufbau entwickelt, mit dem Ziel einer signifikant verbesserten Langzeitstabilität des quantisierenden Magnetfeldes durch Verringerung der Auswirkungen von Temperaturdrifts. Um den temperaturbedingten Drift der Magnetfeldstärke am Ort der eingefangenen Ionen zu kompensieren, wurden Sm_2Co_{17} Magnete mit entgegenwirkenden NdFeB Magneten kombiniert. Infolgedessen konnte die Abhängigkeit des Magnetfelddrifts von der Temperatur um ungefähr 60% verringert werden. Zusätzlich konnte durch technische Massnahmen der Temperaturdrift selbst deutlich reduziert werden. Insgesamt konnte bei einer Langzeitmessung (> 8 h) ein um einen Faktor zehn kleinerer Qubit-Frequenzdrift erzielt werden, ein

sehr vielversprechendes Ergebnis für zukünftige Experimente mit einer hohen Anzahl an Gatteroperationen mit hoher Güte.
Randomised Benchmarking wurde mit dem vorherigen und mit dem verbesserten Permanentmagnetaufbau durchgeführt, um einen direkten Vergleich zu ermöglichen. Die mittlere Einzelqubitgatter Güte nach Wartezeiten konnte signifikant erhöht werden, z.B. für 10 logische Gatteroperationen mit einer Wartezeit von 0.4 ms nach jedem Gatter von 97,3 % auf 99,1 %.

Contents

Chapter 1

Motivation

In the last years, great enhancements have been done in the field of scalable quantum computing with trapped ions. Gate fidelities have been increased above fault-tolerant thresholds [Bal16b]. One of the key challenges is the scaling to sufficient complexity to outperform classical information technology, while the high operation fidelities have to be uphold. The leading candidates for scalable high-fidelity quantum computing platforms are trapped ions and superconducting qubits. Few qubit architectures have been demonstrated for superconducting qubits [Kel15], as well as for trapped ions [Sch13]. Elementary quantum algorithms [Mon16] [Deb16] and fundamental building blocks for performing quantum error correction [Cho14] [Nig14] have been realized. For trapped ions, one scalability problem is the spectral crowding due to $3N$ normal motional modes for N ions. One possibility to overcome this problem, offered the proposal of the *quantum charge-coupled device* (QCCD) [Kie02]. Instead of using one large ion crystal, multiple smaller ion crystals are confined in an array of interconnected Paul traps. In order to realize quantum logic operations on subgroups of qubits, basic shuttling operations have to be implemented: the ion crystal transport, separation and rotation. High fidelity quantum gates require the ions to be close to the motional ground state, which requires the shuttling operations to be operated with low motional excitation. Fast transport without significant coherent excitation has been realized [Bow12] [Wal12], as well as ion crystal separation [Rus14] and swapping of two ions [Kau17a]. General shuttling operations reach higher complexity and therefore, it is crucial to reduce the calibration expense while considering the technical limitations. Additionally, shuttling operations should be performed as fast as possible, to reduce the shuttling induced overhead in the sequences. The present work addresses this problem and provides a first version of a software framework, which automatically generates the voltage ramps, to perform shuttling operations in a linear Paul trap.

While it is of major importance for scalable quantum computing to enhance the performance of shuttling operations, the coherence time is of equally interest. If the system is build upon magnetic field sensitive qubits, dephasing and therefore decoherence is caused by magnetic field fluctuations. This problem can be avoided by the use of ion species with hyperfine structure, for example $^{43}Ca^{+}$ [Ben08][Har14], $^{9}Be^{+}$ [Bol85] or $^{171}Yb^{+}$ [Olm07][Tim11], where the qubit can be encoded in magnetic field insensitive transitions. However, other issues arise for these species, such as the need of large magnetic fields that cause a Zeeman splitting larger than the natural linewidths of

the cycling transitions utilized for Doppler cooling. For some hyperfine species, it is required to use laser fields with a wavelength in the UV range, which are complex to generate and manipulate and lead to resource overhead. In [Rus16], it is shown that it is possible to reach coherence times for the simple-to-operate $^{40}Ca^{+}$ spin qubit in the seconds range. This result was achieved by the combination of a μ-metal enclosure, to reduce external magnetic noise, and Sm_2Co_{17} permanent magnets, to generate the quantizing magnetic field. While the use of permanent magnets compared to the previously used magnetic field inducing coils was very successful, we have observed long-term drifts leading to decoherence. In the present work, the main source of this drift is characterized and an approach to reduce the drift is tested.

This master thesis is structured as follows:

In chapter 2, the theoretical foundations regarding the $^{40}Ca^{+}$ spin qubit, the linear Paul trap and basic shuttling operations are presented. Experimental details of the microstructured segmented ion trap, the multichannel arbitrary waveform generator and the laser setup are described in chapter 3. In chapter 4, the implementation and first experiments with the segmented ion trap control system are presented. Chapter 5 deals with the long-time stability of the quantizing magnetic field and an improved permanent-magnet setup for its generation. To characterize quantum gates, randomized benchmarking, using the first-generation and the newly developed second-generation permanent magnet setup, is demonstrated in chapter 6. The final chapter 7 summarizes the results of this work and gives an outlook on possible next steps for further development of our quantum device.

Chapter 2

Theoretical Foundations

This chapter presents the theoretical foundations of the $^{40}Ca^{+}$ spin qubit, the linear Paul trap and basic shuttling operations.

2.1. The $^{40}Ca^{+}$ Spin Qubit

In our setup, the qubits are realized via $^{40}Ca^{+}$ ions. The relevant atomic transitions are shown in figure 2.1

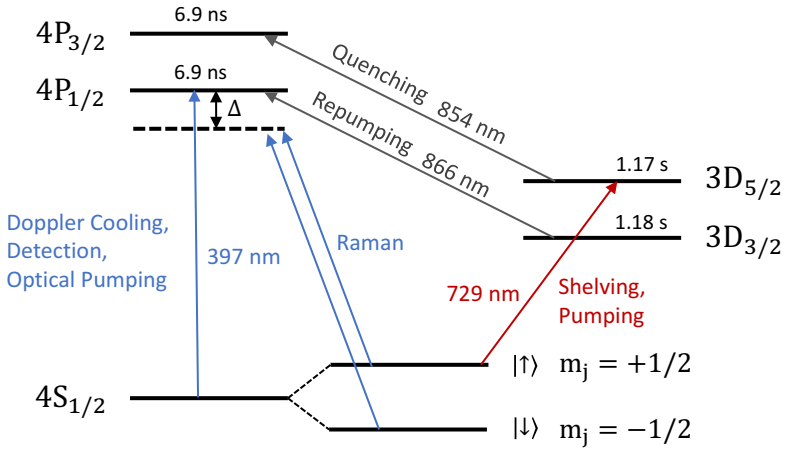

Figure 2.1.: Overview of the relevant atomic levels of $^{40}Ca^{+}$. The qubit is encoded in the Zeeman sublevels of the $4S_{1/2}$ ground state.

The *spin qubit* is formed by the Zeeman sublevels of the $4S_{1/2}$ ground state where $|\uparrow\rangle \equiv |m_j = +1/2\rangle$ and $|\downarrow\rangle \equiv |m_j = -1/2\rangle$. Due to the applied magnetic field, these sublevels are split by around $2\pi \times 10\,\mathrm{MHz}$. The stability of this magnetic field is one of the key topics of this master thesis. The transition between the two qubit states is driven via stimulated Raman transitions. In the following, the realization of the state preparation, state-dependent readout and laser-driven qubit operations are described.

2.1.1. State Preparation

There are two different possibilities to initialize the ion in the desired state ($|\uparrow\rangle$ or $|\downarrow\rangle$) by using optical pumping with light either close to 397 nm or 729 nm and 854 nm. The relevant energy levels are visualized in figures 2.2 and 2.3. In the first process using light close to 397 nm a σ^+ polarized laser beam drives the transition $|\downarrow\rangle \rightarrow |P_{1/2}, m_j = +1/2\rangle$. The $|P_{1/2}, m_j = +1/2\rangle$ state decays within a few nanoseconds back to the ground state $S_{1/2}$, both $|\downarrow\rangle$ and $|\uparrow\rangle$. Due to the fact that only the $|\downarrow\rangle$-state is excited to the $P_{1/2}$-state, the population is transferred to the $|\uparrow\rangle$-state.
In the second process, coherent optical pumping with multiple π-pulses close to 729 nm transfers population from either the $|\uparrow\rangle$ or the $|\downarrow\rangle$ to the metastable state $D_{5/2}$. With an additional laser pulse at around 854 nm the ion can be excited to the short lived $P_{3/2}$ (*Quenching*), which decays back to either $|\uparrow\rangle$ or $|\downarrow\rangle$. The first one decays to either $|\uparrow\rangle$ or $|\downarrow\rangle$, the second one only to the $|\uparrow\rangle$-state. Population accumulates in the qubit state which is not depleted by the coherent excitation on the quadrupole transition.

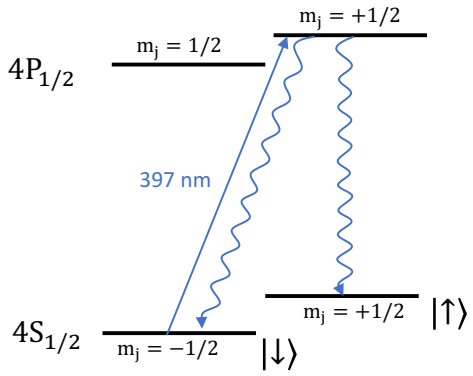

Figure 2.2.: Qubit initialiaization in $|\uparrow\rangle$ using optical pumping.

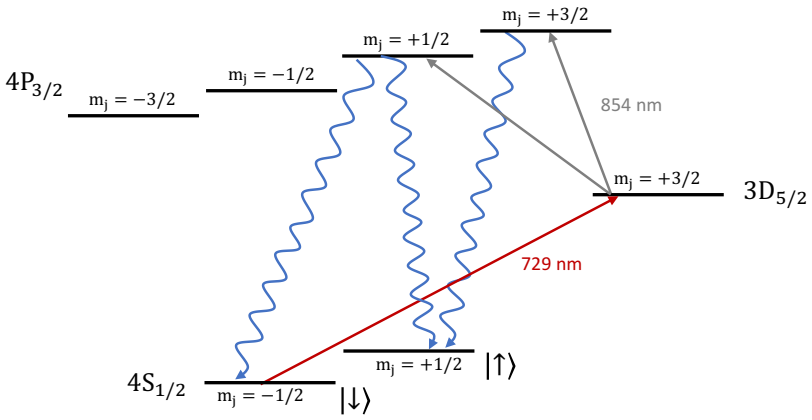

Figure 2.3.: Qubit initialization in $|\uparrow\rangle$ using coherent excitation $\sim 729\,\text{nm}$ and $854\,\text{nm}$.

The transition to the short-lived $|P_{1/2}, m_j = +1/2\rangle$ state is not only used for qubit initialization, but also to perform Doppler cooling of the trapped ions. This cooling technique is based upon the Doppler effect. The light is red detuned to the $S_{1/2} \leftrightarrow P_{1/2}$ transition by a few MHz. In the reference scheme of an ion moving towards the laser beam this light is resonant, the ion absorbs a photon and is excited to the short-lived $P_{1/2}$ state. Due to this detuning, photon scattering is increased if the ion moves towards the laser. As the photons are reemitted on resonance, this leads to energy loss and therefore gives rise to an effective friction. This serves for cooling trapped ions down to the milli-Kelvin temperature regime.

2.1.2. Readout

Readout of the spin qubit is realized via state-dependent electron shelving. A laser pulse resonant to the $|\uparrow\rangle \leftrightarrow 3D_{5/2}$ transition selectively depletes either the $|\uparrow\rangle$ or $|\downarrow\rangle$ state. Then light with a wavelength close to 397 nm is applied to drive the transition $S_{1/2} \leftrightarrow P_{1/2}$. Upon resonant illumination near 397 nm, the quantum state will collapse, and fluorescence will be observed if the ion is projected into the ground state, whereas no fluorescence will be emitted if the ion is projected into the metastable state. There is a probablitity that the $P_{1/2}$-state decays into the metastable $D_{3/2}$-state, which requires repumping to the $P_{1/2}$ by using an additional laser at 866 nm.

2.1.3. Qubit Rotations

Single-qubit operations can be represented as rotations of the state vector on the Bloch sphere [Nie00]. The angles θ and φ define a point on the unit three-dimensional sphere shown in Fig. 2.4.

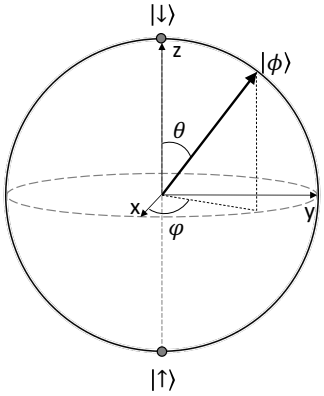

Figure 2.4.: Bloch sphere representation of a qubit.

The state vector can be expressed as

$$|\psi\rangle = \cos\frac{\theta}{2}|\downarrow\rangle + e^{i\varphi}\sin\frac{\theta}{2}|\uparrow\rangle\,. \tag{2.1}$$

An arbitrary single qubit unitary gate operator can be described as a product of rotations. Therefore the resonant driving of a single qubit is given by

$$\hat{R}_\varphi(\theta) = \exp\left(-i\frac{\theta}{2}\left(\hat{\sigma}_x\cos\varphi + \hat{\sigma}_y\sin\varphi\right)\right) \tag{2.2}$$

with Pauli matrices $\hat{\sigma}_x$,$\hat{\sigma}_y$. Experimentally, the rotation angle φ is controlled by the phase of the light field, where the pulse area $\theta = \Omega t$ is defined as the product of the Rabi frequency Ω and the laser pulse time t. The controllable coherent coupling between the qubit levels $|\uparrow\rangle$ and $|\downarrow\rangle$ is induced by simultaneous irradiation of two laser beams, which frequency difference is close to the Zeeman splitting of the qubit energy levels. More details on this stimulated Raman transition are covered in the following chapter.

2.1.4. Light-Motion Coupling

As described earlier, we use different laser systems to perform preparation, cooling, detection and manipulation of the $^{40}Ca^+$ ion. The calculations hereinafter base on the picture of a two-level-system, which is a proper approximation as long as the coupling inducing laser is close to resonance only for this specific two internal levels and the Rabi frequencies are much smaller than the detuning to offresonant transitions [Lei03], which is valid for our spin qubit. The ground state $|g\rangle$ and the excited state $|e\rangle$ are separated by an energy difference of $\hbar(\omega_e - \omega_g) = \hbar\omega_0$. Therefore, the appropriate two-level Hamiltonian $\hat{H}^{(e)}$, taking the rotating wave approximation into account which allows to neglect the rapidly oscillating term proportional to $\omega_e + \omega_g$, is given by

$$\hat{H}^{(e)} = \hbar\frac{\omega_0}{2}\left(|e\rangle\langle e| - |g\rangle\langle g|\right) = \hbar\frac{\omega_0}{2}\hat{\sigma}_z \tag{2.3}$$

where $\hat{\sigma}_z$ is the Pauli-z matrix.
The ion motion in the potential can be expressed in the Heisenberg picture using the ladder operators $\hat{a}$ and $\hat{a}^\dagger$ and the axial trap frequency ω_x

$$\hat{H}^{(m)} = \hbar\omega_x\left(\hat{a}^\dagger\hat{a} + 1/2\right) \tag{2.4}$$

The total Hamiltonian for a single ion coupling to a laser induced electromagnetic field is then described by

$$\hat{H} = \hat{H}^{(e)} + \hat{H}^{(m)} + \hat{H}^{(i)} \tag{2.5}$$

with the interaction Hamiltonian $\hat{H}^{(i)}$. There are three different types of interaction we make use of, the electric dipole allowed transitions, electric quadrupole allowed transitions and stimulated Raman transitions. All these can be handled in a single framework by specifying the Rabi frequency Ω, an effective wave number k and an effective light frequency ω. In the case of dipole and quadrupole transitions these properties ω and k are directly given by the coupling light field, whereas the two light fields driving the stimulated Raman transition result in an effective wave vector of $\boldsymbol{k} \equiv \boldsymbol{k}_1 - \boldsymbol{k}_2$ and an effective light frequency of $\omega \equiv \omega_2 - \omega_1 = \omega_0 + \delta$, while δ is the detuning of ω with respect to the qubit resonance ω_0 (see Fig.2.5).

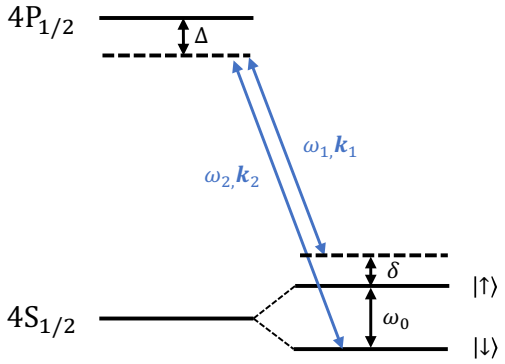

Figure 2.5.: Scheme of the stimulated Raman transition.

$$\hat{H}^{(i)} = \frac{\hbar}{2}\Omega\left(\hat{\sigma}_+ + \hat{\sigma}_-\right)\left[e^{i(\boldsymbol{k}\hat{x}-\omega t+\phi)} + e^{-i(\boldsymbol{k}\hat{x}-\omega t+\phi)}\right] \tag{2.6}$$

whereby $\hat{\sigma}_+ = \frac{1}{2}(\hat{\sigma}_x + i\hat{\sigma}_y)$, $\hat{\sigma}_- = \frac{1}{2}(\hat{\sigma}_x - i\hat{\sigma}_y)$ and the phase of the light field ϕ.
The Lamb-Dicke parameter is defined as $\eta = k\sqrt{\frac{\hbar}{2m\omega_x}}$ and describes the relation between the extension of the ground state wave packet and the wave number of the electromagnetic field along the trap axis x. In the Lamb-Dicke regime the mean

phonon number $\bar{n}$ is small and therefore $\eta \ll 1$. Based on these premises the interaction Hamiltonian can be expressed in the interaction picture in close approximation as [Lei03]

$$\hat{H}^{(i)} = \frac{\hbar}{2}\Omega\left[\hat{\sigma}_+ e^{-i\delta}\left(1 + i\eta\left(\hat{a}^\dagger e^{i\omega_x t} + \hat{a}e^{-i\omega_x t}\right)\right) + h.c.\right]. \tag{2.7}$$

Visualized in Fig. 2.6 is the influence of δ. Depending on this detuning, different transitions according to the motional state highly dominate:

- **Carrier (car)**
  detuning of $\delta = 0$, which induces a transition $|n\rangle|g\rangle \leftrightarrow |n\rangle|e\rangle$ with a Rabi frequency Ω. It does not influence the motional state and is therefore used to perform spin flips.
- **Blue Sideband (bsb)**
  detuning of $\delta = +\omega_x$, which induces a transition $|n\rangle|g\rangle \leftrightarrow |n+1\rangle|e\rangle$ with a Rabi frequency $\Omega_{bsb} \approx \Omega\eta\sqrt{n+1}$. The two-level-system and the motional state are excited and deexcited at the same time.
- **Red Sideband (rsb)**
  detuning of $\delta = -\omega_x$, which induces a transition $|n\rangle|g\rangle \leftrightarrow |n-1\rangle|e\rangle$ with a Rabi frequency $\Omega_{rsb} \approx \Omega\eta\sqrt{n}$. While transferring the two-level-system from ground to excited state the motional state is deexcited and vice versa. Resolved sideband cooling makes use of this to reduce the mean occupied phonon number.

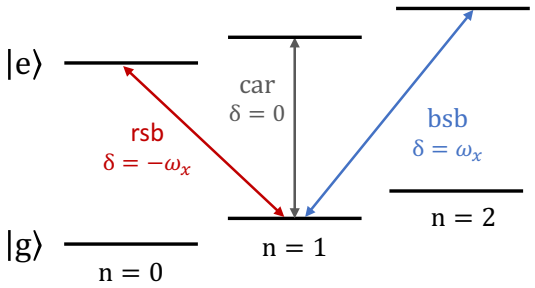

Figure 2.6.: Stimulated Raman transitions in the *Lamb-Dicke regime*. Depending on the detuning δ either the red sideband (rsb), blue sideband (bsb) or carrier (car) transition is driven.

Similarly, it is possible to transform a state $|n\rangle|g\rangle$ to $|n-N\rangle|e\rangle$ and vice versa, using a laser field detuned by $-N\omega_x$ to the qubit frequency ω_0. The effective Rabi frequency, to transfer a state with n phonons in a state with $n \pm N$ phonons, is given by

$$\Omega_{n,n\pm N} = M_{n,n\pm N}\Omega. \tag{2.8}$$

with the matrix elements [Win79]

$$M_{n,n\pm N} = e^{-\eta^2/2}(i\eta)^N \mathcal{L}_n^N(\eta^2) \left(\frac{n!}{(n\pm N)!}\right)^{\pm 1/2} \tag{2.9}$$

and the generalized Laguerre polynomials $\mathcal{L}$. A typical Lamb-Dicke parameter is $\eta = 0.23$. If a transition is driven with a laser frequency close to a sideband, this leads to *Rabi oscillations* for each populated phonon number. For an initially ground state cooled ion, the time dependent population of the excited state $|e\rangle$ can be expressed as

$$p_e(t) = \sum_{n=0}^{\infty} p_n \sin^2\left(\frac{\Omega_{n,n+N}}{2}t\right) \tag{2.10}$$

with the initial phonon distribution function p_n. Therefore, Rabi oscillations can be used as a tool to characterize the motional state of a trapped ion. A fit on multiple sidebands yields enough information to estimate the mean phonon number $\bar{n}$. In the case of higher populated phonon numbers, it is required to assume the underlying phonon distribution p_n, to get a sufficient fit result. We differentiate two kinds of states which are of interest for experiments in ion traps: *coherent states* and *thermal states*.

In segmented ion traps, coherent states are created by acceleration of an ion along the trap axis. The force which displaces the ion can be interpreted classically, due to the much larger spatial extent of the confining potential compared to the wave packet of trapped ions. This classical force induces oscillatory motion, which can be described with a coherent state $|\alpha\rangle$ and a *displacement operator* $\hat{D}(\alpha) = \exp(\alpha\hat{a}^\dagger - \alpha^*\hat{a})$, applied to the vacuum state.

$$|\alpha\rangle = \hat{D}(\alpha)\,|0\rangle \tag{2.11}$$

where the complex number α is the displacement parameter. The phonon number of a coherent state underlies a Poissonian distribution:

$$p_n^{(coh)}(\alpha) = |\,\langle n|\alpha\rangle\,|^2 = \frac{|\alpha|^{2n}}{n!}e^{-|\alpha|^2} \tag{2.12}$$

with the mean phonon number given by $\bar{n}_{coh} = |\alpha|^2$.

If an ion is coupled to a thermal reservoir, the occupation probabilities of the harmonic oscillator states are thermally distributed. For trapped ions, this reservoir is given by the Doppler cooling laser. Another thermal process is the motional excitation due to electrical noise. It follows the occupation probability distribution as

$$p_n^{(th)} = \frac{\bar{n}_{th}^n}{(\bar{n}_{th}+1)^{n+1}}. \tag{2.13}$$

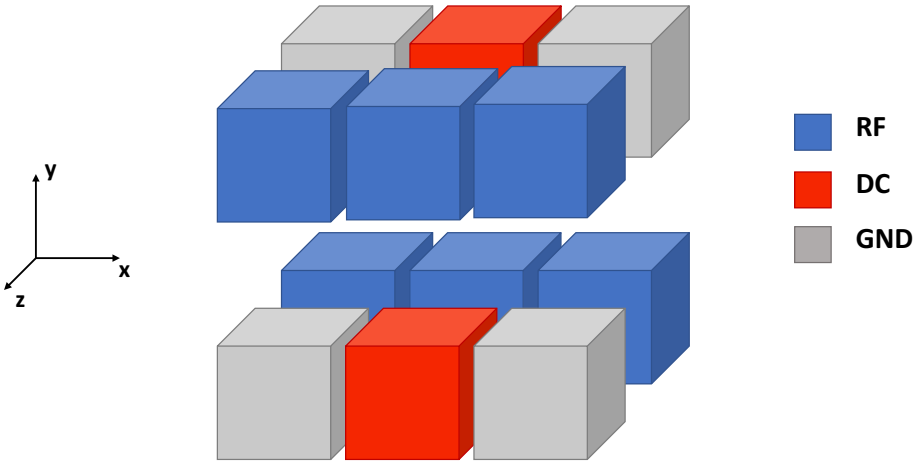

Figure 2.7.: Sketch of a linear Paul trap.

2.2. Linear Paul Trap

The $^{40}Ca^{+}$ ions are trapped in a segmented linear Paul trap, confined in three dimensions x, y, z by applying an alternating current radio frequency (rf), as well as a direct current (dc). The rf and dc electrodes are arranged opposite to each other 2.7 in a way that the rf generates an oscillating quadrupole field that provides confinement in the y and z direction. Confinement in the x direction along the trap axis is provided by the dc electrodes. The total potential along a given direction $q = x, y, z$ can be written as

$$V(q,t) = \alpha_q^{(rf)} q^2 \cos\left(\Omega_{rf} t\right) + \alpha_q^{(dc)} q^2 \tag{2.14}$$

with ion mass m, angular radio frequency Ω_{rf} and potential curvatures $\alpha_q^{(rf)}$ and $\alpha_q^{(dc)}$. The curvatures refer to potentials generated by a voltage of 1 V at the dc/rf electrodes. The origin is set to be centered in x between the dc electrodes in Fig. 2.7 as well as centered in the transverse y, z plane. Compliance to the Laplace equation $\Delta V = 0$ is required individually by dc and rf potential curvatures which leads to

$$\alpha_x^{(rf)} + \alpha_y^{(rf)} + \alpha_z^{(rf)} = 0 \tag{2.15}$$

$$\alpha_x^{(dc)} + \alpha_y^{(dc)} + \alpha_z^{(dc)} = 0 \tag{2.16}$$

For the particular geometry shown in Fig. 2.7 this condition is fulfilled by

$$\alpha_x^{(dc)} = \alpha_y^{(dc)} = -2\alpha_z^{(dc)} \equiv \alpha^{(dc)} \tag{2.17}$$

and

$$\alpha_y^{(rf)} = -\alpha_z^{(rf)}, \alpha_x^{(rf)} = 0 \tag{2.18}$$

Note that $\alpha_x^{(rf)} = 0$ and therefore the potential along the x axis does not depend on the rf. This allows modifying the potential to perform shuttling operations along the trap axis by the use of the dc electrodes. The equation of motion for a single positive charged particle follows in the form of three uncoupled Mathieu differential equations

$$\frac{\mathrm{d}^2 q}{\mathrm{d}\tau^2} + (a_q - 2b_q \cos(2\tau))\, q = 0 \tag{2.19}$$

$$\tau = \frac{\Omega_{rf} t}{2} \qquad a_q = \frac{4|e|\alpha_q^{(dc)} U_{dc}}{m\Omega_{rf}^2} \qquad b_q = \frac{2|e|\alpha_q^{(rf)} U_{rf}}{m\Omega_{rf}^2} \tag{2.20}$$

where $q = x, y, z$. A stable solution of this equations in the limit of $a_q < b_q^2 << 1$ was calculated as [Lei03]

$$q(t) \approx q_0 \cos\left(\gamma_q \frac{\Omega_{rf} t}{2}\right)\left(1 + \frac{b_q}{2}\cos\left(\Omega_{rf} t\right)\right) \tag{2.21}$$

with $\gamma_q = \sqrt{a_q + b_q^2/2}$. This describes a *secular harmonic motion* with a frequency of $\gamma_q \Omega_{rf}/2$ superimposed by the *micromotion*, a rapid small amplitude oscillation at a frequency Ω_{rf}.

If we now consider a chain of N ions in the trap, the motion along the trap axis x is influenced by a harmonic potential generated by the trap electrodes and the Coulomb force, which describes here the repulsion of equally charged particles. The ions are strongly confined in y and z direction by the alternating rf field and confined in x direction by a harmonic potential. The potential energy of a chain of N $^{40}Ca^{+}$ ions is given by [Jam98]:

$$V = \sum_{m=1}^{N} \frac{1}{2} M_{Ca} \omega_x^2 x_m(t)^2 + \sum_{\substack{n,m=1 \\ m \neq n}}^{N} \frac{e^2}{8\pi\epsilon_0} \frac{1}{|x_n(t) - x_m(t)|} \tag{2.22}$$

where M_{Ca} is the mass of a calcium ion, e the electron charge, ϵ_0 the vacuum permittivity and ω_x the angular trap frequency, characterizing the strength of the trapping potential in axial direction. The equilibrium positions $x_m^{(0)}(t)$ of the ions can be determined by

$$\left[\frac{\partial V}{\partial x_m}\right]_{x_m = x_m^{(0)}} = 0 \tag{2.23}$$

2.3. Shuttling Operations Along Trap Axis

As further described in chapter 3.1, the segmented ion trap yields 32 equally spaced electrode pairs along the trap axis x, where in principle each of these pairs can constitute a linear Paul trap. The total axial potential is given by a linear superposition of the electrostatic potentials generated by each electrode:

$$\Phi(x) = \sum_i U_i \Phi_i(x) \tag{2.24}$$

Here U_i is the voltage at segment i and $\Phi_i(x)$ represents the potential at position x when the electrode pair pertaining to segment i is set to 1 V and all other electrode pairs are set to 0 V. We consider only positions along the rf node of the trap, i.e. $y, z = 0$. Fig. 2.8 shows the electrostatic potentials calculated for the ion trap used for this work.

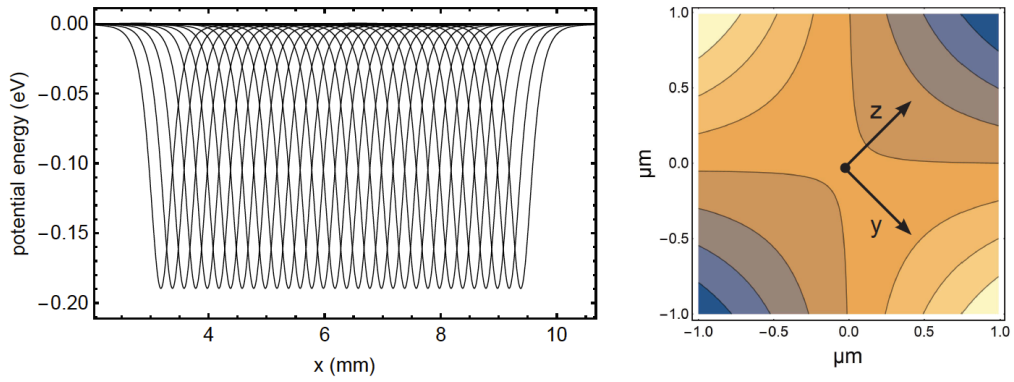

Figure 2.8.: Electrostatic potentials calculated for the ion trap used for this work. Left: Axial potential wells for each of the 32 electrode pairs at a voltage of -1 V, while all others are set to 0 V. Right: A single ion located in the center of the static radial potential. The confinement in z direction is stronger than in y direction due to an asymmetric trap geometry in radial direction. Simulation and plot from [Kau17c].

The trap frequency at a potential minimum position x_{min} with $\Phi'(x_{min}) = 0$ and $\Phi''(x_{min}) > 0$ is given by

$$\omega_x = \sqrt{\frac{e}{M_{Ca}} \Phi''(x_{min})} \tag{2.25}$$

2.3.1. Transport of Trapped Ions

Transport of an ion from one segment to another is implemented by ramping up the voltage at the electrode pair where the ion was confined at the beginning and simultaneously ramping down the voltage at the neighbouring electrode pair in the transport

direction. This moves the axial potential well along the trap axis. It has previously been demonstrated that this transport can be performed on a μs timescale with negligible energy increase [Wal12][Bow12]. The motional excitation can be characterized by a well defined phase, because it is a harmonic oscillation. In [Wal12], the transport has been realized over a segment to segment distance of 280 μm, within the timescale of a few oscillation cycles. With the help of a voltage "kick" on a neighbouring segment, with respect to the target segment, a motional excitation of less than one phonon could be achieved. This is possible with a well calibrated phase and amplitude of the voltage pulse, due to the oscillatory nature of the excitation. However, for experimental setups with multiple ions and many shuttling operations this is not feasible due to the calibration effort for each shuttling operation and the influence of this voltage pulse on other ions in the trap.

2.3.2. Separation of Ion Crystals

Another essential building block to realize scalable quantum information protocols is the separation of an ion crystal [Hom06]. We approximate the potential along the trap axis x by a Taylor expansion around the initial center of mass position of the crystal, which is valid as long as the ion distance is small compared to the segment size [Kau14].

$$\Phi(x,t) \approx \beta(t)x^4 + \alpha(t)x^2 + \gamma(t)x \tag{2.26}$$

The coefficients α, β and γ are predetermined by the trap geometry and the time dependent voltages applied to relevant segments, which are the center segment at voltage U_C, the two split segments at U_S and the two outer segments at U_O. Fig. 2.9 shows the important intermediate steps of the ion crystal separation process. C is the center segment, where the ions are initially located, surrounded by the left and right split segments S, and the left and right outer segment O.

$$\alpha(t) = U_C(t)\alpha_C + U_S(t)\alpha_S + U_O(t)\alpha_O + \alpha' \tag{2.27}$$
$$\beta(t) = U_C(t)\beta_C + U_S(t)\beta_S + U_O(t)\beta_O + \beta' \tag{2.28}$$
$$\gamma(t) = \Delta U_S(t)\gamma_S + \Delta U_O(t)\gamma_O + \gamma' \tag{2.29}$$

The α_i, β_i and γ_i with $i = \{C, S, O\}$ are determined by the second, fourth and first derivatives of the corresponding electrode potentials at $x = 0$. $\Delta U_S(t)$ and $\Delta U_O(t)$ are given by the difference of the voltages applied on the respective electrode pairs. Experimental imperfections can be taken into account by the offset coefficients α', β' and γ'. In case a residual field γ' along the trap axis breaks the symmetry and is sufficiently strong enough that both ions stay confined in one of the potential wells throughout the separation process, this can be compensated with tilt voltages ΔU_S and ΔU_O. In the initial situation, the ions are confined in a harmonic trap potential with $\alpha \gg 0$, and the trap frequency is given by $\omega = 2e\alpha/M_{ca}$. To separate the ion crystal, α is smoothly ramped from a positive to a negative value (see Fig. 2.9). The

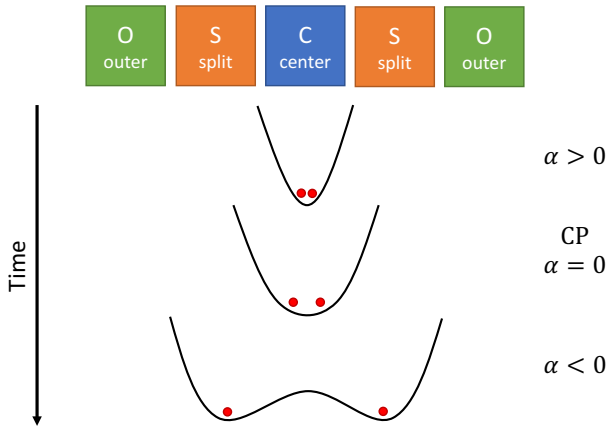

Figure 2.9.: Sketch of the process of ion crystal separation. The ions are initially confined in a strong harmonic potential ($\alpha > 0$). By changing the voltages U_C, U_S and U_O at the respective electrode pair, the harmonic potential is first transferred into a predominantly quartic one ($\alpha \approx 0$) and finally to a double-well potential ($\alpha < 0$).

critical point (CP) is the point were $\alpha = 0$, where the axial confinement assumes a minimum. However, some harmonic confinement persists: Due to the Coulomb repulsion, the ions are not located at $x = 0$, and due the the quartic coefficient β, $\Phi'' > 0$ at the ion locations. In order not to excite the ions, the rate of change of α has to be small around the critical point [Rus14]. Including the Coulomb repulsion, the total potential of a two-ion crystal with ion distance d can be written as

$$\Phi_{tot}(x_0, t) = \Phi(x_0 + d/2, t) + \Phi(x_0 - d/2, t) + \frac{e}{4\pi\epsilon_0 d} \tag{2.30}$$

Following the argumentation above, it is useful to maximize β at the critical point.

Chapter 3

Experimental Setup and Methods

3.1. Microstructured Segmented Ion Trap

The design and fabrication of the trap shown in Fig. 3.1 and used in this master thesis is further described in [Kau17c].

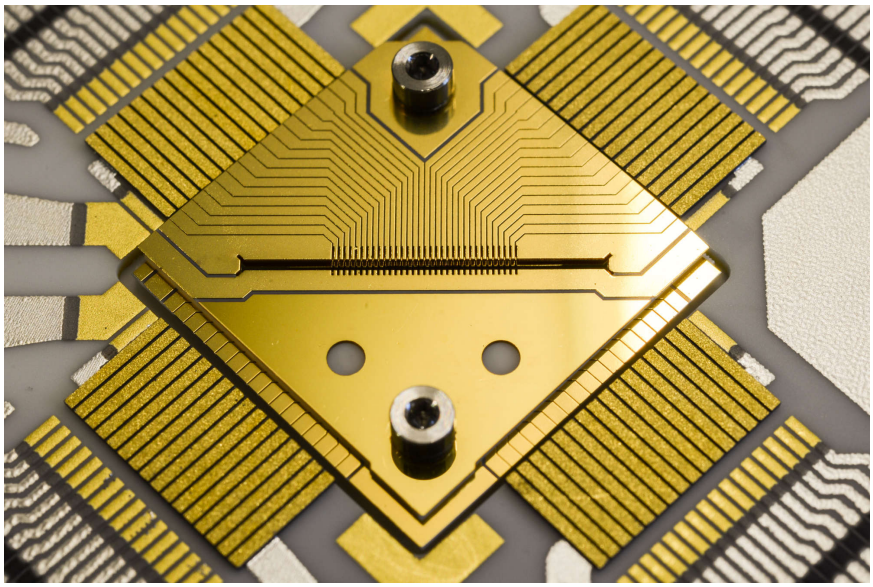

Figure 3.1.: Picture of the trapped-ion quantum processor which is used to perform the experimental tasks of this thesis [Kau17c].

The trap was designed to provide low motional heating, easy optical access and to allow fast shuttling operations. The trapping region consists of 32 trapping electrode pairs. Each trapping zone forms a linear Paul trap as described in section 2.2. Segment 20 is the so-called laser interaction zone (LIZ), where all the lasers are focused on the segment center position. More detailed information on the lasers and their purpose can be found in section 3.3. For a typical dc trapping voltage of -6 V at segment 20 and 0 V at all other segments, the axial trap frequency is given by $\omega_x \approx 2\pi \times 1.49\,\mathrm{MHz}$. At a typical rf drive frequency of around 33 MHz and a peak-to-peak voltage of around 320 V, the radial frequencies result as $\omega_y \approx 2\pi \times 3.8\,\mathrm{MHz}$ and $\omega_z \approx 2\pi \times 4.6\,\mathrm{MHz}$. Our

setup provides low heating rates for these trap frequencies. Mean phonon numbers are $\bar{n}_x \approx 12(5)$phonons/s, $\bar{n}_y \approx 15(5)$phonons/s and $\bar{n}_z \approx 6(5)$phonons/s, recently measured by Vidyut Kaushal.

3.2. Multichannel Arbitrary Waveform Generator

The 32 dc electrode pairs are supplied by a custom made fast multichannel arbitrary waveform generator. This generator is FPGA-based and capable of supplying voltage in the range of $\pm$ 40 V with a resolution of about 16 bit/1.2 mV for each electrode. The minimal time to set the voltages simultaneously at all segments is 380 ns, which results in a voltage update rate of ∼2.6 MSamples/s. The maximum slew rate is determined by a measurement of the time necessary to change the voltage on a channel from -10 V to 10 V and results as 14 V/μs. To suppress electrical noise, each channel features a second order II-type low-pass filter with a cutoff frequency of currently 50 kHz. These technical specifications are fundamental input parameters for the software framework presented in section 4. In addition to 80 analog output channels, the arbitrary waveform generator provides 24 digital output channels with an update rate of 50 MSamples/s. These are used to trigger time dependent tasks during a measurement sequence, including aquisition of data with the EMCCD (Electron Multiplying Charge-Coupled Device) and PMT (Photomultiplier Tube), as well as the VFG (Versatile Frequency Generator)[1]. The VFG provides a rf signal, which is used to tune the lasers via AOMs (Acusto Optical Modulators).

Figure 3.2.: Picture of the custom multichannel arbitrary waveform generator.

[1] VFG-150, TOPTICA Photonics

3.3. Overview of the Laser System

For operation of the $^{40}Ca^{+}$ spin qubit, multiple lasers are required (see Sec. 2.1). Specifications and orientation relative to the trap axis are described in the following.

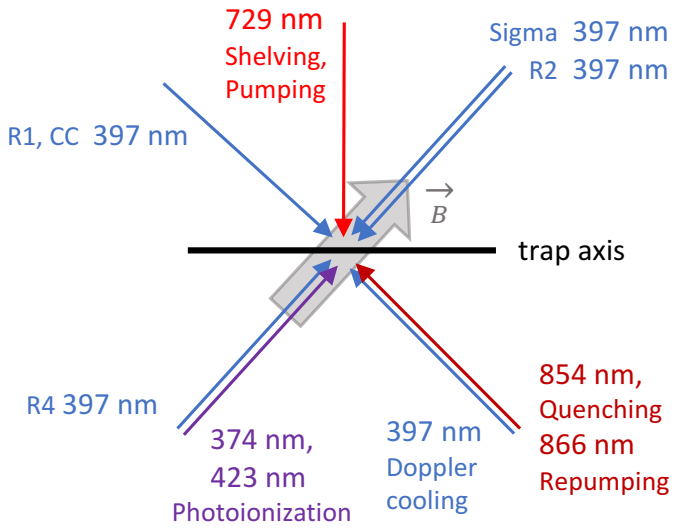

Figure 3.3.: Beam alignment in our setup relative to the trap axis.

Photoionization - 423 nm and 374 nm

To ionize the neutral ^{40}Ca atoms, which are emanated by an effusive calcium oven, a two-photon ionization is used. The diode laser at 422.791 nm is regulated using the wavemeter[2], while the diode laser at 374 nm serves the ionization to the continuum and therefore does not require frequency stabilization. Both lasers are coupled to the same single-mode fiber.

Doppler Cooling, Fluorescence Detection and Optical Pumping - 397 nm

The cycling transition $S_{1/2} \leftrightarrow P_{1/2}$ is driven by a single mode laser near 397 nm. A beam from a single extended cavity diode laser (ECDL) source, stabilized to a linewidth of roughly 1 MHz via a Pound-Drever-Hall (PDH) lock on an external cavity [Bla01], is split into two beams. These two beams are seperately controlled by two AOMs in double pass configuration. One of the beams is used for optical pumping during resolved sideband cooling and therefore has to be circularly polarized.

[2]Wavelength Meter WSU, HighFinesse Laser and Electronic Systems

Repumping and Quenching - 866 nm and 854 nm

The repumping single mode laser drives the $D_{3/2} \leftrightarrow P_{1/2}$ transition, in order to empty the long living $D_{3/2}$ state to the short living $P_{1/2}$ state during Doppler cooling, after readout decay and after pumping to the $D_{3/2}$ (see Sec. 2.1). The single mode laser driving the $D_{5/2} \leftrightarrow P_{1/2}$ transition is necessary to reinitialize the qubit after a "dark" $|\uparrow\rangle$ state detection. The qubit is in the metastable state $D_{5/2}$, from where it can be reinitialized to the $S_{1/2}$ by driving the dipole transition $D_{5/2} \leftrightarrow P_{3/2}$, from where the qubit decays back to the ground state, which is called *Quenching*.
Both lasers are controlled by AOMs in double pass configuration. Frequency drifts of the repump laser are compensated by the PDH stabilization, while the frequency stability of the linear polarized quenching laser is of less importance, it is regulated via a wavemeter to an accuracy of about 10 MHz.

Spin Readout and Initialization - 729 nm

The quadrupole transition $S_{1/2} \leftrightarrow D_{5/2}$ is driven by a single mode laser source near 729 nm. To suppress coupling to the axial ion motion, this laser is aligned at an angle of 90 °. Power and frequency of the light is controlled using an AOM in a double-pass configuration. Stabilization with the PDH technique [Bla01] to a high-finess cavity provides a linewidth of less than 1 kHz [Mac12]. The laser is in parallel with the quantizing field polarized and thus couples to $\Delta m = 0, \pm 2$ transitions [Roo00].

Stimulated Raman Transitions - 397 nm

To allow coupling to different motional modes, stimulated Raman transitions are driven by four laser beams R1, R2, R4 and CC, all generated by the same single mode laser close to 397 nm and detuned by multiples of the natural linewidth of around 130 MHz to the $S_{1/2} \leftrightarrow P_{1/2}$ transition. The important distinction between the beam paths R1, R2, R4 and CC is the alignment according to the trap axis (see Fig. 3.3). They are used in four different combinations to obtain different purposes (further described in [Kau17c]):

- R1 & CC : Aligned in a co-propagating configuration. The effective $\vec{k}$ vanishes, which leads to decoupling of the ion motion while driving stimulated Raman transitions between the qubit states $|\uparrow\rangle$ and $|\downarrow\rangle$, which is favourable for qubit rotations.

- R1 & R2 : Coupling to the coaxial motion with a Lamb-Dicke factor of 0.2 to 0.25. These beams are utilized for axial sideband cooling and measurement of the axial motion.

- R1 & R4 : Coupling to the radial motion with a Lamb-Dicke factor of 0.1 to 0.15. This configuration is utilized for radial sideband cooling and measurement of the radial motion.

- R4 & CC : Spin dependent light force, which is used to implement an entangling gate operation [Bal16b].

3.4. Experimental Control Software

All experimental setups in the AG Schmidt-Kaler are controlled by the C++ based Master Control Program (MCP) in combination with a highly setup-specific dynamic link library (usullay called *Script.dll*), which underlies continuous development. The MCP uses APIs to interact with the hardware devices and provides a graphical user interface (GUI) for control of experimental hardware and measurement parameters and for displaying measurement data. Within this work, a new software layer was developed, integrated into the Script.dll and tested. This layer is supposed to offer the possibility for automated dynamical position of trapped ions in the context of multi-qubit operations. Fast ion crystal separation, merging and movement into, as well as out of, the laser interaction zone is required. Modelling the trap potential is achieved by controlling the voltages on the 32 DC segments. Whatever this can lead to large complexity where the experimentalist has to take into account surrounding potential wells of stored ion crystals while programming the voltage waveform to e.g. move another ion crystal into the LIZ. To perform larger shuttling operations build out of a set of operations as separation and movement over a range of one segment, symmetry potentials are applied to achieve a symmetric potential along the trap axis. Further details on successful four-quit sequences implemented using this technique can be found in [Kau17c]. These symmetry potentials impede the scalability when going to a higher number of qubits, due to the limited space along the trap axis and the voltage ramping, that needs valuable measurement time as well as large effort to prepare new measurement schemes.

Chapter 4

SITCONS - Segmented Ion Trap Control System

The major part of the work underlying this thesis is the development of a C++ library, that allows automated control of generic shuttling operations on multi-qubit registers in segmented ion traps. This chapter describes the motivation and requirements (Sec. 4.1), explains how the software works (Sec. 4.3) and shows first measurements performed using the automated control system (Sec. 4.5).

4.1. Motivation and Design Goals

So far, shuttling operations were realized by concatenation of predefined building blocks. This is not desirable for the following reasons:

- Shuttling operations for complex sequences cause a huge programming effort, for example $\sim$ 2000 lines of code to implement the four-qubit entanglement [Kau17b].
- The concatenation of predetermined operations leads to suboptimal shuttling operations, for instance a stepwise adiabatic transport of single ions over several segments. Therefore, shuttling operations consume $> 90\%$ of the valuable time budget for the execution of a given quantum algorithm.
- More difficult shuttling operations, as the direct transfer of an ion from one crystal to a neighbouring one have to be divided into multiple building blocks: separation, transport and merging.
- The space available along the trap axis is not used efficiently. Due to the presence of additional potential wells used to compensate surrounding potential wells, e.g. during the very tilt sensitive separation process and due to larger distances between stored ion crystals to minimize the influence of the potential wells on each other.
- In case of hardware changes, such as the low pass filters, the arbitrary waveform generator or the trap chip itself, it is not easy to re-use the existing sequences.

According to the above-mentioned reasons, it is imperative in the sense of scalability to provide a software framework, that automatically generates voltage ramps. In the first step of realizing this software, we include the following restrictions:

I.I Ions shall only be shuttled along the trap axis of a linear Paul trap, $y, z = 0$. Junctions, which have been realized in T [Hen06], X [Bla09][Wri13] or Y [Shu14] geometry, are not yet taken into account.

I.II We assume the symmetry of a three dimensional Paul trap, therefore the rf node shall always be at $y, z = 0$, which restricts the usability of this first version of the software for surface traps.

I.II Ion movement is restricted to the x axis, therefore crystal rotations [Kau17a] are not yet covered by the software framework, and the ion ordering is fixed. However, crystal rotations can still be manually added to sequences.

In order to generate suitable voltage ramps, the software should meet the following requirements:

II.I Voltage ramps are to be generated based on realistic trap potentials.

II.II The only required input information consists of the positions of the ions inside the trap at intermediate steps during a given experimental sequence.

II.III All relevant technical details of the setup are to be taken into account. These are the voltage limit of the arbitrary waveform generator, the slew rate and the low pass filters (see Sec. 3.2).

II.IV The optimization of the voltage ramp requires frequent access to the trap potential at a given position. Therefore, the potential shall be numerically represented in an efficient way, which also provides means for accurate calculation of the derivatives to calculate forces and trap frequencies.

4.2. Approximation of the Segmented Ion Trap Potential

The automated positioning control is based upon an optimization process of the applied dc voltages at the trap electrodes, with respect to the trapping potential, especially the position of the minima and the curvature at this points. Fundamental for this optimization is the underlying approximation of the potential, which is described in the following. The simulation of the microstructured trap was done by Henning Kaufmann using the *boundary element method* based BEM-Solver developed by Kilian Singer [Sin10].
To fulfill requirement II.IV (Sec. 4.1), the result of this simulation is approximated for each segment i with a rational function for the Φ_i in Eq. (4.1)

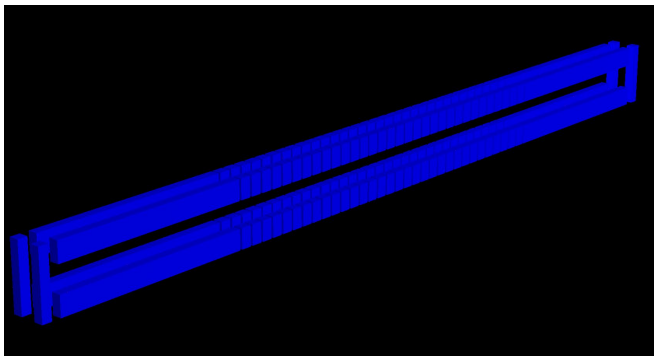

Figure 4.1.: Trap design used for the simulation. As compared to the real trap, only the endcaps contain minor disparities for simplification.

$$\Phi_i(x) = \frac{\sum_{j=0}^{N^{(i)}} u_j (x - x_0^{(i)})^j}{\sum_{j=0}^{N^{(i)}} v_j (x - x_0^{(i)})^j} \tag{4.1}$$

The coefficients describing the nominator and denominator polynomials, u and v, are stored and used by SITCONS to calculate the potential during the optimization process, which is specified hereinafter. The reference position $x_0^{(i)}$ corresponds to the potential maximum of each of the Φ_i, and the polynomial orders $N^{(i)}$ are chosen to provide a sufficient fitting accuracy at the absence of spurious zeros of the denominator, which would lead to singularities of the potential and its derivatives.

4.3. Voltage Ramp Calculation

In the following, the basic steps to generate suitable voltage ramps, the underlying optimization algorithm, details of the objective function and the mapping of the sets of voltages to a certain time step are described.

4.3.1. Steps of Voltage Ramp Generation

Fig. 4.2 shows the very basic steps of a voltage ramp generation. The indispensable input parameters are the *Positions* and *Curvatures* of the initial and final potential *Wells*. The Wells related to one ramp step, which means are present at the same time, are organized in a *WellSet*. An interpolation between the initial and final WellSet, with a given number of intermediate steps, is stored in a ramp of WellSets: *Ramp<WellSet>*. The optimization takes this ramp, covering the position and curvature information for every potential Well at a certain step in the sequence, and determines the voltages according to the above described requirements (Sec. 4.1). The result is a *VoltageSet*, that stores the voltage information for each of the 32 electrode pairs at a given ramp step. The first version of SITCONS focuses on the optimization of appropriate voltage ramps.

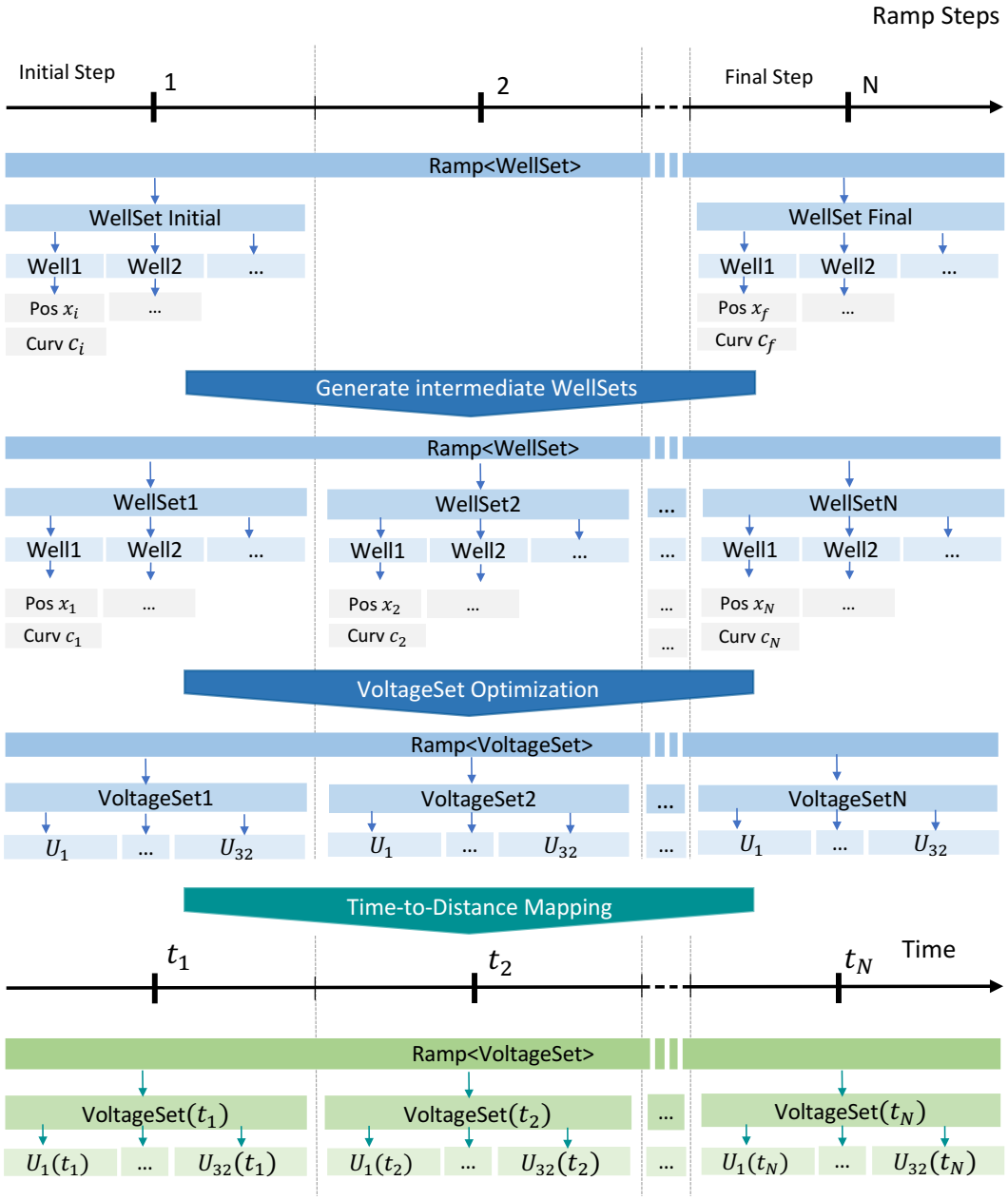

Figure 4.2.: Sketch of the basic steps of generating a voltage ramp. Steps related to the optimization of the voltage ramps are blue, the step where the voltage ramps are adjusted to satisfy a time-to-distance function is green. The important input information, position and curvature of each potential well, is stored in a *Well*. All Wells at one ramp step are organized in a *WellSet*. Given an initial WellSet and a final WellSet and the number of interpolation steps N, intermediate WellSets are generated. The optimization determines a suitable *VoltageSet*, which includes a voltage information for each of the 32 electrode pairs. In the next step, these voltage sets are processed to generate the desired position-time relation (see Fig. 4.5).

4.3.2. Nelder-Mead Optimization Algorithm

An indispensable part of SITCONS, is the optimization algorithm in combination with the highly setup-specific objective functions, for performing the VoltageSet determination. The optimization algorithm used here is a simplex method for function minimization first published by J.A. Nelder and R. Mead in 1965 [Nel65]. The *Nelder-Mead* algorithm minimizes a single-valued *objective* function of several variables, where knowledge of the gradient is not required. The main idea is to evaluate the given objective function for a set of points forming the simplex, which at minimum should consist of $n+1$ vertices to optimize in n-dimensional parameter space. The objective function is evaluated at all vertices, and subsequently the simplex is altered according to a fixed set of rules to converge into a local optimum. The exact optimization flow is illustrated in Fig. 4.3.
To generate a potential well, the set of voltages at all segments is optimized for every time step, according to the predefined position and curvature of the potential at this particular position and time. A test point $\boldsymbol{x}$ in the Nelder-Mead flow chart corresponds to a set of voltages including all 32 segments. $f(\boldsymbol{x})$ is the objective function, which takes a set of voltages $\boldsymbol{x}$ and returns a score. The SITCONS library is designed such that the optimization algorithm itself can be exchanged with manageable effort by another algorithm. Of higher importance is the objective function, which is specialized in the case of transport and separation of ion crystals. In the following both particular cases will be outlined. The reason for choosing the Nelder-Mead algorithm in the first place, was its robustness and flexibility. It is capable of performing a local nonlinear optimization and can be extended to take technical boundary conditions into account, while it is not necessary to know the gradient of the underlying objective function.

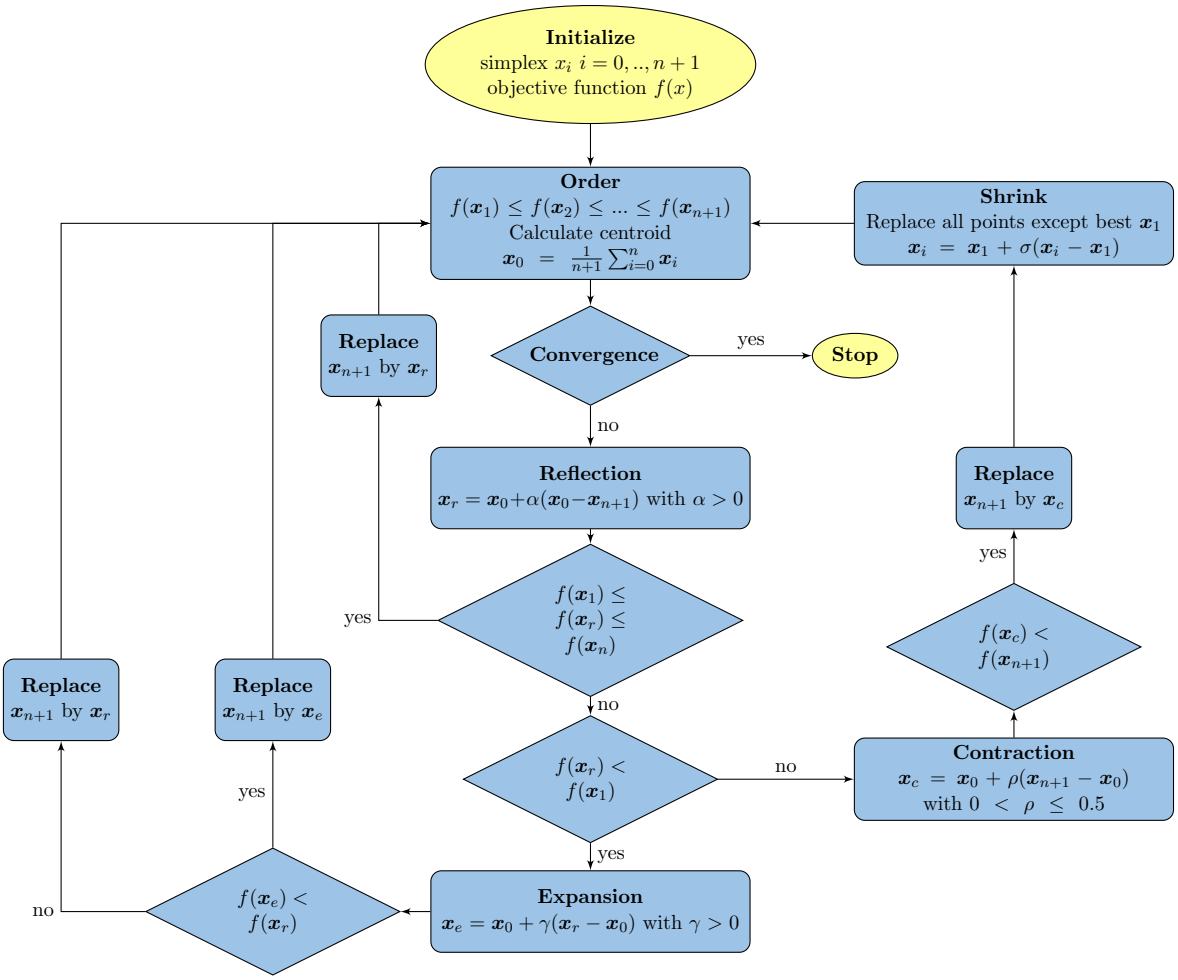

Figure 4.3.: Flow chart of Nelder-Mead optimization algorithm.

4.3.3. Optimization of Transport Voltage Ramp

The aim of the new method is to realize a more efficient, quasi-ballistic transport. The transport voltage ramps generated with SITCONS are consistent with the following conditions:

- Only the segments in a range of 1.5 times the segment width to an ion shall be active, i.e. those are allowed to be set to another voltage than 0 V.
- The voltage steps shall be within the technical limitations (see Sec. 3.2).
- The distance of the new ion equilibrium position compared to the last position shall be small in every step of the voltage ramp.
- The voltages shall generate a harmonic potential and keep the local axial trap frequency at the ion position constant.

The new method allows to adjust voltages at three segments to form a potential well with a given curvature. The voltage of the center segment is not fully predetermined by this condition, there are several solutions to generate the given curvature of the trapping potential in the potential minimum. To overcome this problem, several additional constraints are implemented in the objective function.
The objective function used in the Nelder-Mead algorithm is given by

$$F_{Transport}(\boldsymbol{U}) = \sum_n w_n p_n(\boldsymbol{U}) \tag{4.2}$$

with input set of voltages $\boldsymbol{U} = \{U_1, U_2, ..., U_{32}\}$, penalties p_n and weights w_n. The penalties and weights are defined as follows:

Potential well positions: p_0**,** $w_0 = 10^{13}$

This part of the score function makes sure that potential wells are located at the specified positions. This is done by minimizing the force generated by all segments at every position. N_w is the number of Wells in the corresponding WellSet, i the segment index and c_j the reference curvature in the minimum x_j of each Well:

$$p_0 = \sum_{j=0}^{N_w} \left(\frac{\sum_{i=1}^{32} U_i \Phi_i'(x_j)}{c_j} \right)^2 \tag{4.3}$$

Potential well curvatures: p_1**,** $w_1 = 10^6$

This part of the score enforces predefined curvature values at the given well positions. The curvature defines the local trap frequencies. The optimization minimizes the

squared difference of the total second derivative of the potential at the specified well positions and the specified curvature.

$$p_1 = \sum_{j=0}^{N_w} \left(\frac{\sum_{i=1}^{32} U_i \Phi_i''(x_j) - c_j}{c_j} \right)^2 \tag{4.4}$$

Voltage: p_2**,** $w_2 = 10^{-1}$

The optimization is biased to low absolute values for the voltages, in order to keep the voltage values away from the limit U_{lim}. Note that this part of the score function counteracts the curvature part p_1, which requires finite voltages to generate potential wells of given curvature.

$$p_2 = \left(\frac{\sum_{i=1}^{32} |U_i|}{U_{lim}} \right)^2 \tag{4.5}$$

Voltage ramp first derivatives: p_3**,** $w_3 = 10^2$

The change in voltage, compared to the last step is preferred to be small, in order to avoid conflicts with bandwidth and slew-rate limitations. Only used if previous voltage information exists. $\tilde{U}_i$ is the previous set of voltage at segment i.

$$p_3 = \left(\frac{\sum_{i=1}^{32} \sqrt{(U_i - \tilde{U}_i)^2}}{U_{lim}} \right)^2 \tag{4.6}$$

Voltage ramp second derivative: p_4**,** $w_4 = 10^2$

The change in voltage, compared to the second last step is preferred to be small, in order to avoid conflicts with bandwidth and slew-rate limitations. Only used if second previous voltage information exists. $\tilde{\tilde{U}}_i$ is the second previous set of voltage at segment i.

$$p_4 = \left(\frac{\sum_{i=1}^{32} \sqrt{(2\tilde{U}_i - U_i - \tilde{\tilde{U}}_i)^2}}{U_{lim}} \right)^2 \tag{4.7}$$

Voltage boundaries for segment activation and inactivation: p_5**,** $w_5 = 10^{-1}$

Only segments within a given range of a specified potential well are active, which means are allowed to be set to another voltage than 0 V. Otherwise, the optimization would put remote segments at voltages close to the limit voltage U_{lim}, as the electric field feedthrough is decreasing with the segment distance to the position of interest. b_i

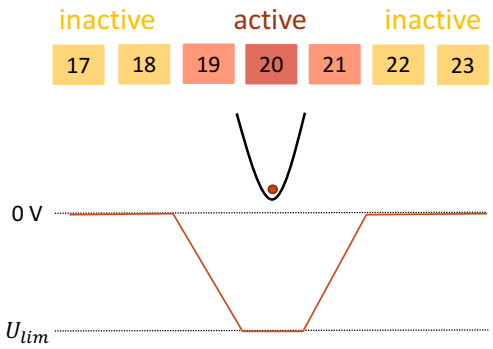

Figure 4.4.: Maximum allowed absolute voltage at corresponding segment distance to a potential well position.

is the upper bound for the allowed voltage at segment i. It ensures a smooth junction between active and inactive segments (Fig. 4.4).

$$p_5 = \left(\frac{\sum_{i=1}^{32} (b_i - U_{lim}) U_i}{U_{lim}} \right)^2 \tag{4.8}$$

Voltage slew rate limit: p_6, $w_6 = 10^3$

This penalty is zero, unless the change in a voltage during a ramp step exceeds the slew rate. s is the given slew rate and t_{step} the time per ramp step.

$$p_6 = \sum_{i=1}^{32} \max(0, |\tilde{U}_i - U_i| - s \cdot t_{step}) \tag{4.9}$$

Center voltage calibration: p_7, $w_7 = 10^3$

At the laser interaction zone, every optimization process should finally lead to the same voltage configuration, in order to keep the radial trap frequencies constant, which is of high importance for driving entangling gates. If the new equilibrium position is in the range of $\pm 5\,\mu$m to the LIZ, the voltage at the center segment is supposed to converge to a preset value. This penalty is zero, unless a reference well position x_j is within $5\,\mu$m of the laser interaction zone at segment 20 with position x_C and U_C the calibrated center voltage and U_{20} the respective element of the voltage set under consideration.

$$p_5 = \begin{cases} \sum_{j=0}^{N_w} |U_{20} - U_C| & \text{if } |x_c - x_j| < 5\,\mu\text{m} \\ 0 & \text{else} \end{cases} \tag{4.10}$$

4.3.4. Temporal Optimized Voltage Ramp

The *ramps steps*, at which the resulting voltage sets are defined, have the meaning of a quasi-time, i.e. the ramp step defines the progress of the particular shuttling operation from the initial to the final specified potential well configurations. Note that between any two specified potential well configuration, the ramp steps correspond to linear motion of the potential well. This does not necessarily correspond to linear change of the ion positions, as these might depend nonlinearly on the well positions when the Coulomb interaction between the ions is taken into account, see Sec. 4.6. Voltage sets between integer ramp steps can be obtained via interpolation.
The subsequent processing step to obtain voltage ramps, which are to be actually generated and applied to the trap electrodes, is then to find a mapping from the ramp steps to an actual time coordinate. This mapping has to fulfill the condition of being continuous, and it would be desirable to have the ramp step monotonously increasing with time. While the implementation of this second optimization step is beyond the scope of this thesis, we briefly discuss how this is to be carried out, and illustrate the mapping with an example.
As for the voltage ramp generation, the automated generation of optimized time mappings requires a score functional. As one seeks to keep motional excitation from shuttling low, one could implement an integrator for solving the equations of motions of the ions comprising the register, and optimize on the final total energy. Furthermore, the time domain voltage ramps are subject to further technical limitations, therefore it will be necessary to optimize on low bandwidth and to make sure that the voltage change rates are compatible with the maximum slew rate of the employed waveform generator.
We illustrate the concept of time mapping by considering the most simple example of shuttling an ion from location d_i to d_f within time τ. Simulations in [Rus12] pointed out, that a $\sin^2$ shaped trajectory of the potential well is favourable. The expected excitation is lower, the ion is moved slowly at the beginning and at the end of the shuttling process, while a faster shuttling in between reduces the total required time. Therefore, the transfer function of the potential well position is chosen to be

$$d(t) = d_i + (d_f - d_i) \sin^2 \left(\frac{\pi t}{2\tau} \right) \tag{4.11}$$

with $t \in [0, \tau]$, τ being the overall transport time and an initial position d_i and a final position d_f.

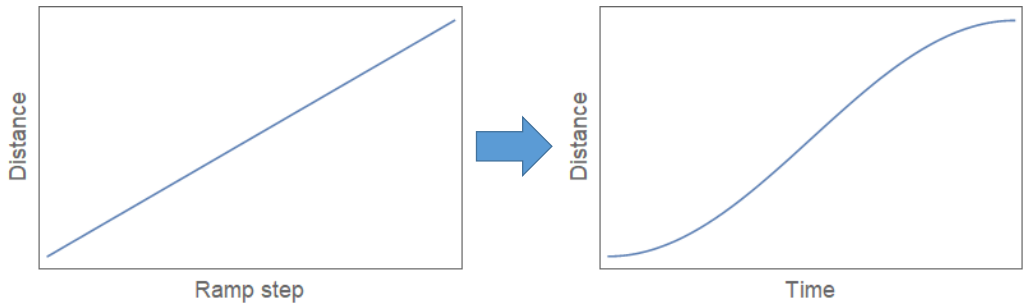

Figure 4.5.: Illustration of mapping a distance-vs-ramp step function to the time domain via a sine-squared transfer function.

4.4. Automated Multi-Segment Transport

The transport over multiple segments is a typical shuttling operation in our quantum logic processor. In the following, a transport over ten segments is generated with SITCONS and compared to the voltage ramp of the previously used transport scheme. To experimentally realize the shuttling of a single ion across multiple segments, as described in section 2.3.1, time-dependent voltage ramps have to be computed. So far, multi-segment shuttling has been realized by concatenated adiabatic transport from one segment to the next, which is rather inefficient due to the repeated acceleration and deceleration.
Fig. 4.6 shows different transport ramps to perform a transport from segment 20 to segment 10 with the so far used transport scheme, as well as voltage ramps generated with SITCONS. For the STICONS generated ramps, the voltage at segment 20 (LIZ) is calibrated to the result of an optimization for a single ion at the trap center to -7.2079 V. In case there are no other potential wells present, this leads to a voltage of -2.9488 V at segment 19 and -2.9465 V at segment 21. If there are surrounding potential wells, the voltages at segment 19 and 21 are automatically adjusted during the optimization. It can be seen, that the previous transport ends after every segment in the initial configuration of 0 V,-6 V,0 V, before the transport to the next segment is started. The transport ramp generated with SITCONS, especially optimized on the required transport over 10 segments provides a smooth change in the equilibrium position without stopping in between. The upper voltage ramp is as well generated with SITCONS and based on the one shown in the middle graph, mapped to a time dependent function of the transport distance (see Sec. 4.3.4).

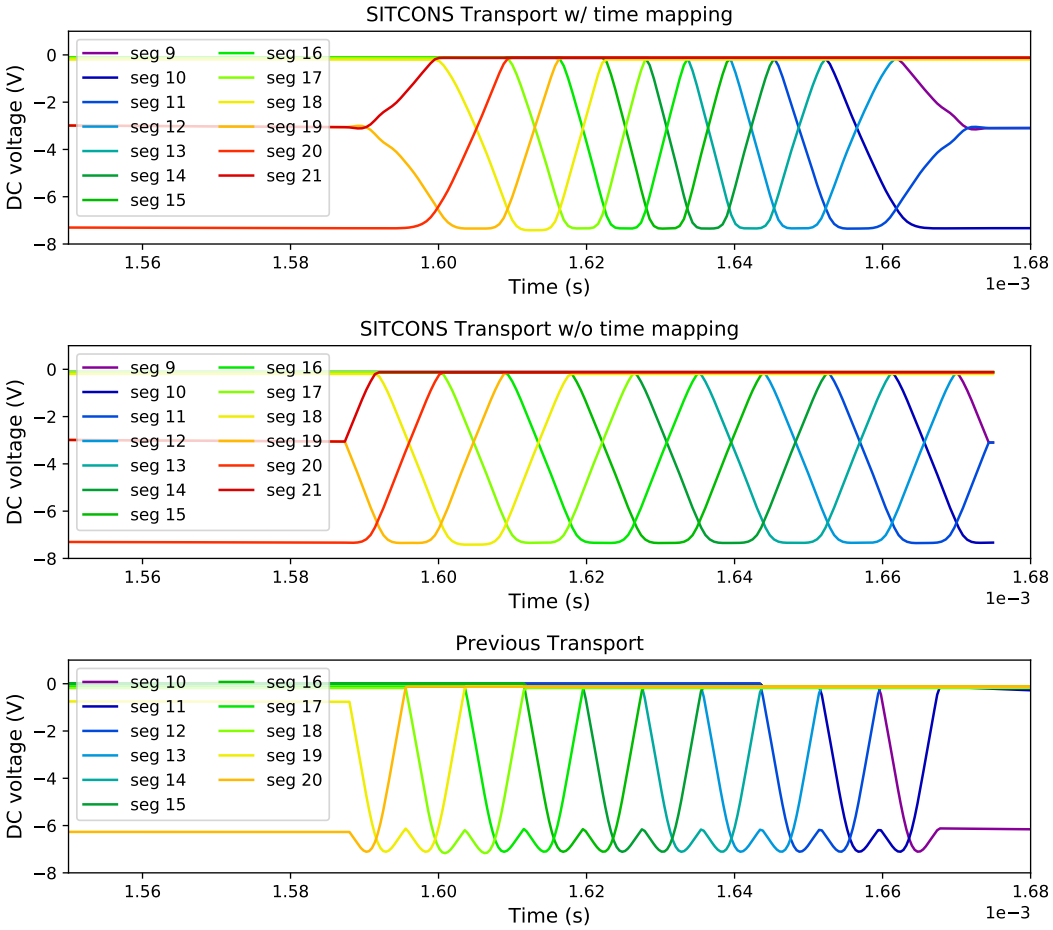

Figure 4.6.: Comparison of voltage ramps that achieve a transport from segment 20 (LIZ) to segment 10 within 100 μs. The upper two graphs show voltage waveforms generated by SITCONS where the lower graph shows the transport segment by segment as it was done previously.

4.5. Experimental Characterization of the Multi-Segment Transport

In the following, measurements to characterize the transport of a single ion over multiple segments are described and the results are presented. To make sure that SITCONS produces voltage ramps, which perform a fast transport with low motional excitations, the motional state of the ion after transport is investigated.

4.5.1. Excitation on the Radial Modes of Motion

To get a qualitative idea of the motional excitation on the two radial modes, a single ion is initialized in the $|\uparrow\rangle$-state and is Doppler and resolved sideband cooled. A transport from segment 20 (LIZ) to segment 10 is performed with varying preset transport time per segment. In case of a transport with time mapping of the transport distance to time as a $\sin^2$ function, this time is the average time used per segment. Note that especially for short durations of a few μs per segment, the real time will be a bit longer due to filters between arbitrary waveform generator and electrode pairs. The voltages are updated at maximum rate, which is equal to a simultaneous update on all segments every 380 ns. After a ring off time of 50 μs at segment 10, the ion is transported back to segment 20. Then a π-pulse with the respective Raman laser beams R1 and R4, to couple to both radial modes (details see Sec. 3.3), is performed on the red sideband (rsb) or blue sideband (bsb). In case the number of phonons after the transport is $n > 1$, the π-pulse on the red sideband transfers the qubit into the $|\downarrow\rangle$-state, which leads to a bright ion detection, whereas for the motional ground state $n = 0$, this transition is forbidden. The qubit stays in the $|\uparrow\rangle$-state and the ion detection result is dark (see Fig. 4.7).
This sequence is performed 500 times and the average probability, that the detection results in a bright ion is shown in Fig. 4.8 for the radial mode in y direction and in Fig. 4.9 for the radial mode in z direction. In both figures, the result of a transport generated with the above described previous transport scheme and the transport generated with SITCONS is compared. The SITCONS transport corresponds to the center plot in Fig. 4.6 without time mapping.
For both radial modes, it is shown that the transport does not excite the motional state down to a preset transport time per segment of $\sim 3.5\,\mu$s, which is equivalent to a preset total duration of $\sim 35\,\mu$s. The motional ground state is identified by a bright probability close to 0 % for the rsb and at the same time close to 100 % on the bsb. In the case of SITCONS generated voltage ramps, the motional ground state is present for preset transport times of around 1 μs less per segment. To identify the effect for smaller transport times an additional measurement without a pulse on the rsb or bsb is presented in Fig. 4.10. It shows the average bright probability of 500 measurements for preset transport times lower than 3.2 μs for a single ion, which is initialized in the dark state, transported and shelved. In an ideal case, the result is expected to be close to 0 %. In this measurement, the increase in the bright probability appears around the same time, in comparison with the data with π-pulse on the red sideband.

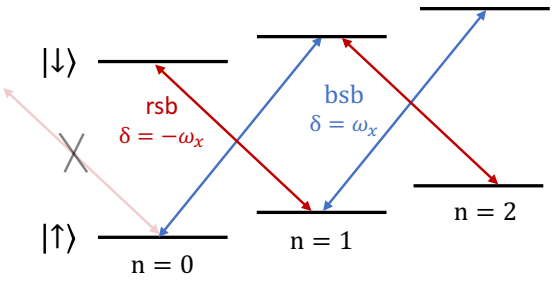

Figure 4.7.: Stimulated Raman transitions in the *Lamb-Dicke regime*. Depending on the detuning δ either the red sideband (rsb), the blue sideband (bsb) or the carrier (car) transition is driven. For $n = 0$ a π-pulse on the rsb can not transfer the $|\uparrow\rangle$-state to the $|\downarrow\rangle$-state.

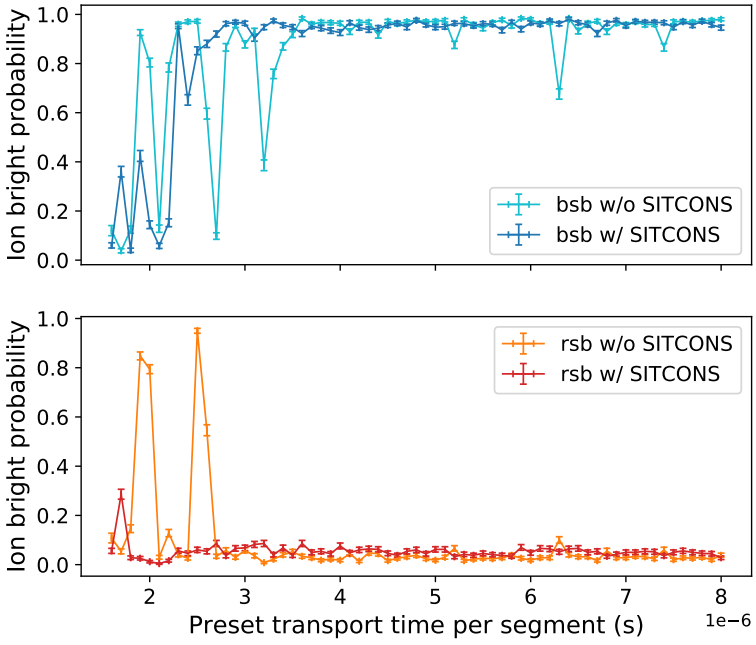

Figure 4.8.: Average bright probability of 500 detections after a transport over ten segments is performed within the given preset transport time per segment. Upper/Lower: π-pulse after transport on bsb/rsb, resonant to radial mode in y direction.

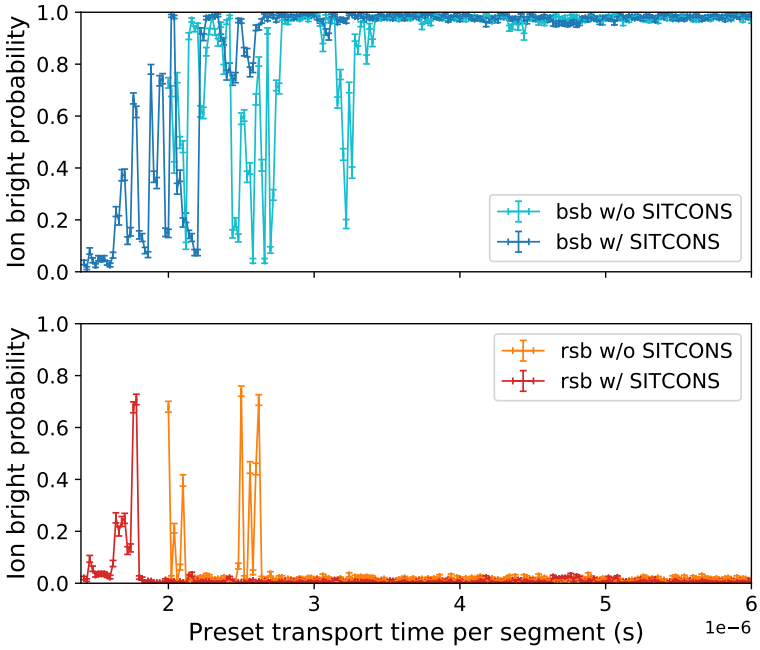

Figure 4.9.: Average bright probability of 500 detections after a transport over ten segments is performed within the given preset transport time per segment. Upper/Lower: π-pulse after transport on bsb/rsb, resonant to radial mode in z direction.

Therefore, we can assume that arises from an imperfect state preparation and readout error (SPAM) and that it is not caused by motional excitation due to the transport. In addition, this absence of motional excitation on the radial modes indicates a very well alignment of the trap. A possible attempt to reduce the SPAM error could be to enhance the alignment of the laser close to 729 nm driving the quadrupole transition $S_{1/2} \leftrightarrow D_{5/2}$, which is used for shelving and initialization.

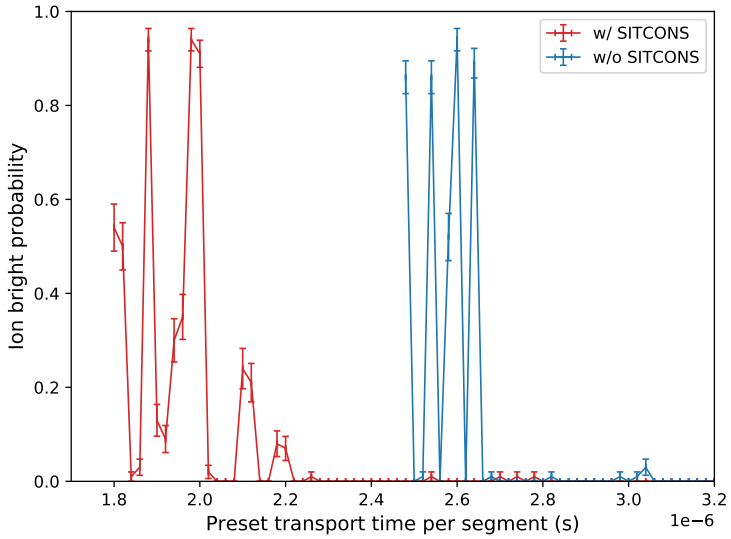

Figure 4.10.: Test of the shelving for different preset transport times w/ and w/o SITCONS. Average bright probability of 500 detections after a transport over ten segments is performed within the given preset transport time per segment.

4.5.2. Excitation on the Axial Mode of Motion

To analyse the axial mean phonon number $\bar{n}$ after a fast transport over multiple segments, the phonon number dependent coupling strength of three transitions is utilized. Therefore, we drive Rabi oscillations, as described in Sec. 2.3.1. First a single ion is trapped, initialized to the $|\uparrow\rangle$ state and ground-state cooled. Then a transport from segment 20 to segment 10 and back is performed. The respective Raman laser beams R1 and R2 are used to couple to the axial mode (details see Sec. 3.3). The effective light frequency is calibrated to be resonant to the carrier, the rsb or the second rsb transition, followed by a state sensitive readout of the spin-qubit. This sequence is repeated each 100 times for different irradiation times of the Raman lasers, to receive the time dependent occupation probability. To obtain a cold transport, the time per segment is typically chosen to be within 30 to 50 μs. To emphasize the difference of the two transport ramps and get transport induced coherent excitation, the following measurements use a shorter transport time of 10 μs

per segment. The mean phonon number of the coherent state depends on the wait time between the initial and the back transport. To enable comparison, the time between the transports is first calibrated to a maximum $\bar{n}$, which results in 3.99 μs for the transport with SITCONS and 4.14 μs for the segment per segment transport without SITCONS. The results are presented in Fig. 4.11, with and without using SITCONS. The coherent and thermal mean phonon numbers $\bar{n}_{coh}$ and $\bar{n}_{th}$ can be estimated by a simultaneous curve fit of the carrier, first and second red sideband with respect to the probability distributions described in Sec. 2.3.1. As expected, the coherent excitation exceeds the thermal excitation in both cases. The coherent excitation of $\bar{n}_{coh} = 15 \pm 1$ after the transport generated with SITCONS is significantly smaller than the coherent excitation of $\bar{n}_{coh} = 244 \pm 9$ after a similar transport with the previously used scheme, where the ion is moved segment by segment. This is a very promising outcome in the direction of faster shuttling, while providing low coherent excitation, especially to reduce the overall shuttling time in large quantum computational sequences.

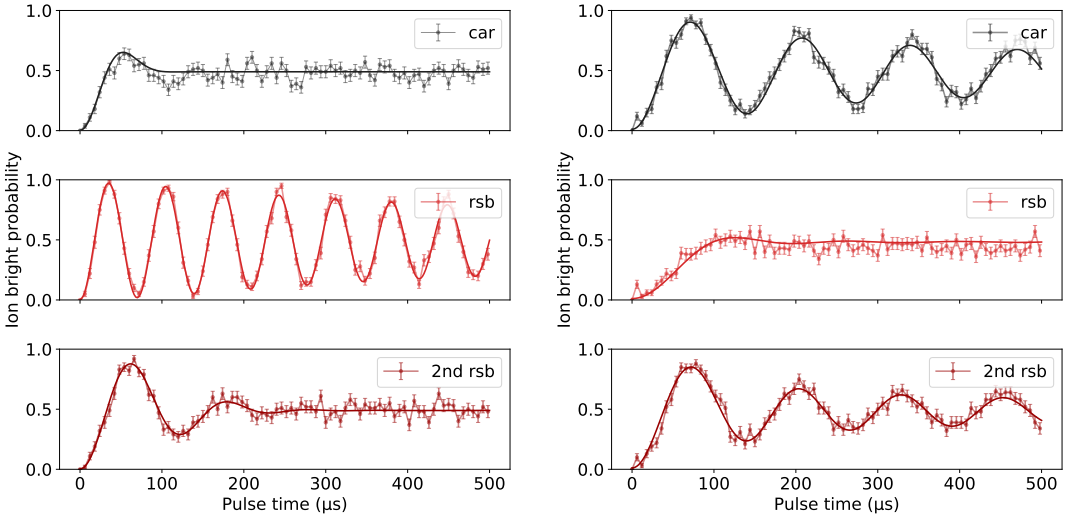

Figure 4.11.: Rabi oscillations for a ground-state cooled ion after a back and forth transport over 10 segments, within 10 μs per segment. Left: the transport ramp is generated with SITCONS. Mean phonon numbers are $\bar{n}_{coh} = 15 \pm 1$ and $\bar{n}_{th} = 0.22 \pm 0.07$. Right: the transport ramp previously used. Mean phonon numbers are $\bar{n}_{coh} = 244 \pm 9$ and $\bar{n}_{th} = 1.3 \pm 0.1$. The solid lines show the output of the simultaneous fits.

4.6. Automated Ion Crystal Separation

This section is about the application of SITCONS for a more complex task than transport, the ion crystal separation process described in Sec. 2.3.2. First, the implementation which is currently in use, further described in [Kau14] and [Rus14], is

presented. On this basis, the conditions on the automatically generated separation voltage ramps are elaborated and the results are presented. The suitable voltage ramps to perform a separation of a two-ion crystal have to be designed according to the double-well potential parameters α, β and γ of Eq. (2.26). This simplified model is used, in order not to be dependent on a precise knowledge of the electrostatic trap potential, but on quantities which can be measured with manageable effort. In the following, we assume a perfectly compensated tilt potential, such that $\gamma = 0$. The approach is based on the definition of the optimum voltages at the initial position with the harmonicity parameter $\alpha_i > 0$, the critical point where $\alpha_{CP} = 0$ and the final position with $\alpha_f < 0$. Ramping the curvature at the center position from positive to negative value corresponds to a transformation of the single-well potential to a double-well potential. Initially the voltages are $U_C^{(i)} < 0$ and $U_O^{(i)} = U_S^{(i)} = 0$. The condition defining the CP is $\alpha_{CP} = 0$, which can be realized by choosing U_S and U_C accordingly. This leaves one degree of freedom, which can be eliminated by maximizing β_C. The largest possible β_{CP} can be calculated by solving Eq. (2.27) for U_C

$$U_C = \frac{1}{\alpha_C} \left(\alpha - \alpha_O U_O - \alpha_S U_S \right), \tag{4.12}$$

setting $U_O^{(CP)} = +U_{lim}$, $U_S^{(CP)} = -U_{lim}$ to the defined maximum voltage and inserting this in Eq. (2.28):

$$\max_{U_C, U_S} \beta_{CP} = \left(\beta_0 + \frac{\beta_C}{\alpha_C} \alpha_S - \beta_S - \frac{\beta_C}{\alpha_C} \alpha_O \right) U_{lim} \tag{4.13}$$

The voltages for the final configuration are chosen to ensure confinement in the centers of the split segments with $U_C^{(f)} = U_O^{(f)} = 0$ and $U_S^{(f)} = -U_{lim}$. The voltage sets for given ramp steps are then obtained by interpolating between these predefined voltage sets. In [Kau14] it is shown, that a minimum possible acceleration at the CP is needed to achieve a low energy transfer. The distance of the ions to be separated is varied regarding a function $d(t)$, which satisfies $d(0) = d_i$, $d(T) = d_f$ and $\dot{d}(0) = \dot{d}(T) = 0$ with initial distance d_i (usually 2 to 4 μm), final distance d_f (usually 400 μm) and total separation time T. A possible choice for $d(t)$ is a sine-square function:

$$d(t) = d_i + (d_f - d_i) \sin^2 \left(\frac{\pi t}{2T} \right) \tag{4.14}$$

To finally obtain time-dependent voltage ramps $U_n(\alpha(d(t)))$, the $\alpha(d)$ relation is computed using trap potentials from simulations. In this previously employed approach, only the five closest electrode pairs are taken into account to calculate the separation voltage ramp. If a two-ion crystal separation takes place, while other ions are stored along the trap axis, symmetry potential wells have to be ramped for compensation, in order to perform the separation with the previously calibrated parameters. This leads to a voltage ramping overhead and costs valuable measurement time. This illustrates that the manual specification of voltage ramps from predefined building blocks can hardly be applied for distributed multi-qubit registers. The physical reason for this is

the long range of the electrostatic forces of the trap segments, which cannot be seen as *local* control fields. Therefore, we see from this particular case why an automated system for voltage ramp generation is utterly required.
The new segmented ion trap control system is able to automatically generate voltage ramps to perform fast ion crystal separation with respect to surrounding potential wells, because every step optimizes on the whole voltage set including all 32 segments. First, the potential well information at the separation center position is copied, such that the initial WellSet contains two Wells at the separation center position, equal in position and curvature. Then intermediate WellSets are generated, to move these two potential wells apart until the final position is reached. The optimization process with the Nelder-Mead algorithm (see Sec. 4.3.2) is performed for every step based on the initial voltages or the last optimized step, until a minimum score is found. The objective function for calculating the score used in the Nelder-Mead algorithm, is of the same form as Eq. (4.2) for the transport generation, with input set of voltages $\boldsymbol{U} = \{U_1, U_2, ..., U_{32}\}$, penalties p_i and weights w_i. The penalties p_1 to p_5 are the same as described for the transport optimization (Sec. 4.3.3), with adjusted weights: $w_0 = 10^{13}, w_1 = 10^3, w_2 = 10^{-1}, w_3 = 10^2, w_4 = 50, w_5 = 0.1$. For the potential wells which move apart during the separation process, it is favourable to optimize the curvatures at the ion position with the attempt to keep them constant, because it ensures that the center voltage is ramped from negative to positive value in order to create a potential barrier between the ions. In contrast to the transport, it is not possible to keep the curvature constant over the whole separation process. Therefore, the corresponding weight w_1 is reduced, not to affect the separation adversely. The weight w_4 is reduced, because it counteracts a large voltage change and ion crystal separation requires to ramp to high voltages close to the critical point. One additional separation specific penalty is added by:

Maximum quartic confinement at near critical point: p_7, $w_7 = 10$

For α close to the critical point, maximize β.

$$p_7 = \begin{cases} 1/\beta & \text{if } |\alpha| < 10^6 \\ 0 & \text{else} \end{cases} \tag{4.15}$$

Fig. 4.12 shows the obtained voltage at segments 18 to 21 during the separation process versus ramp steps, in the case of no surrounding potential wells. The number of interpolation ramp steps was chosen to be 100 in this case. While the generation of transport voltage ramps is based on a simulated trap potential, the more complex ion crystal separation takes additional calibrated parameters $\alpha_{C,S,O}$, $\beta_{C,S,O}$, $\gamma_{S,O}$ into account. For demonstration purposes, the geometry parameters $\alpha_{C,S,O}$, $\beta_{C,S,O}$, $\gamma_{S,O}$ for our trap are taken from [Rus14]. SITCONS automatically uses the quantities of the latest calibration, stored in the master control program.
The requirements specified in the objective function to generate suitable separation voltage ramps differ from the transport ones as follows:

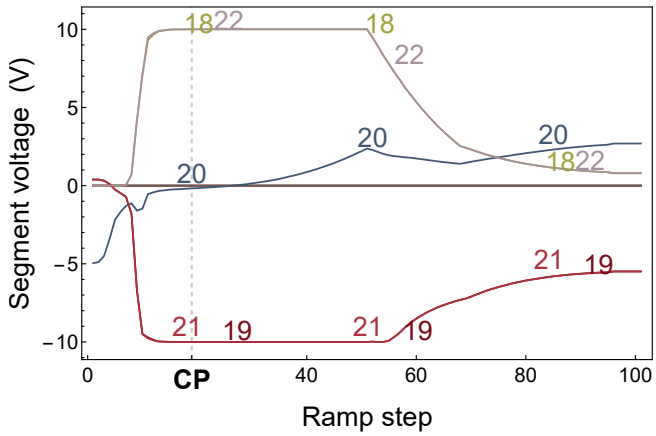

Figure 4.12.: Voltage ramp to separate a two-ion crystal within 100 steps, generated by SITCONS. The numbers in the graph correspond to the trap segment, to which the voltage is applied: The (C)enter segment 20, the (S)eparation segments (19,21) and the (O)uter segments (18,21). Close to the critical point (CP), indicated by the vertical line, the voltages are changed slowly to perform a separation with low energy transfer.

- Only the segments in a range of 2.5 times the segment width to an ion shall be active, which means they are allowed to be set to another voltage than 0 V.
- The distance of the new ion equilibrium position compared to the last position shall be small in every step of the voltage ramp.
- Close to the critical point, the quartic confinement parameter β shall be maximized.

Every requirement is added to the score including a weight, which can be adjusted until the optimized voltage ramps lead to satisfying separation results.

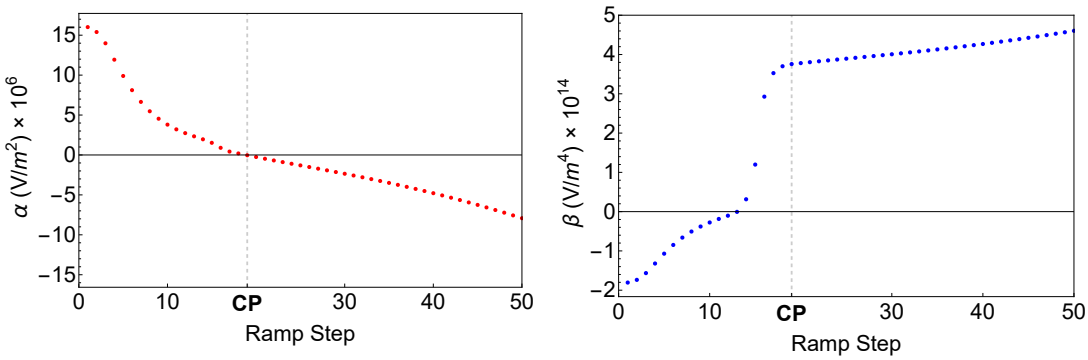

Figure 4.13.: Parameter α and β with respect to the voltages in Fig. 4.12.

Fig. 4.13 shows the harmonic parameter α and the quartic parameter β according to the voltages in Fig. 4.12 and Eq. (2.27), (2.28). As required, α monotonically decreases, and the rate of decrease is reduced with lower gradient around the CP, while β is highly increased and close to its maximum value before the CP is reached. Fig. 4.14 shows how the ions are smoothly separated, whereas Fig. 4.15 displays how the potential is changed by the voltage ramp.
The automatically generated separation voltage ramps satisfy the above requirements. Since it is already fully implemented in the software, it can be characterized in future measurements and used as a building block to reduce the overhead in quantum information protocols.

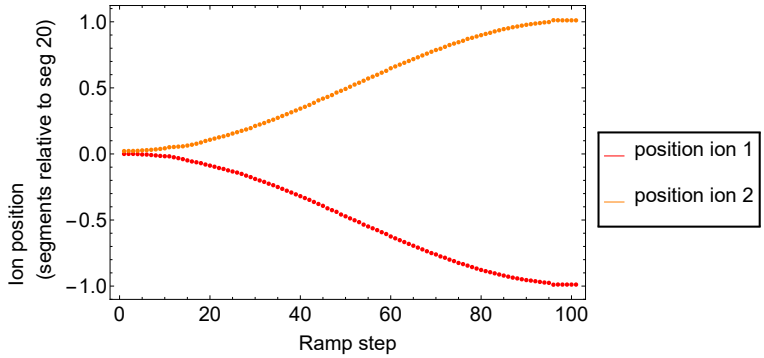

Figure 4.14.: Ion equilibrium position during separation.

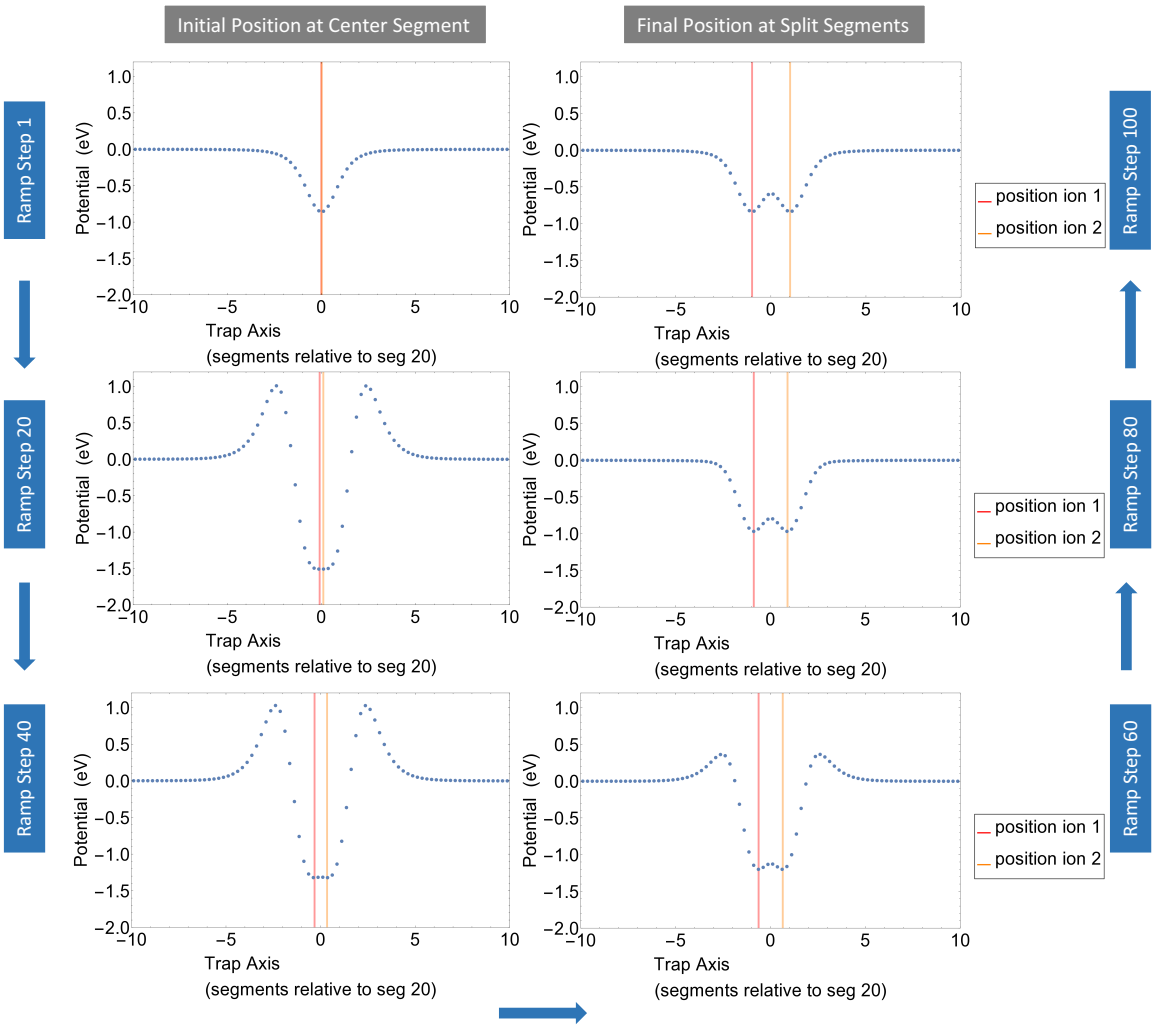

Figure 4.15.: Separation of a two-ion crystal within 100 steps generated by SITCONS. The plotted potential is calculated according to the optimized voltage set of every step and equation (2.26). In the left upper plot, both ions are in their initial position close to the center segment. During the first 40 steps, the ions begin to move slowly apart, while confined in between potential barriers. In ramp step 60 it can be seen, that the potential barriers outside are ramped down, after each ion resides in its own well. At the same time the potential barrier at the center segment start to rise. Up to the final ramp step 100, the minima of the potential wells are moved to the split segments 19 and 21 and the outer potential barriers are totally ramped down again.

Chapter 5

Magnetic Field Drift

We encode the quantum information in the Zeeman-split sublevels of the $4S_{1/2}$ ground state as $|\uparrow\rangle \equiv |4S_{1/2}, m_j = +1/2\rangle$ and $|\downarrow\rangle \equiv |4S_{1/2}, m_j = -1/2\rangle$ (see Sec. 2.1). Therefore, the qubit transition is first-order magnetic field sensitive, which means the magnetic field stability becomes crucial, but it also offers the ability to perform dc magnetometry as was recently shown by Thomas Ruster [Rus17a]. This chapter describes an analysis of the long-time stability of the quantizing field and a second-generation permanent magnet setup for its consequential improvement.

5.1. Permanent Magnets

Permanent magnets generate a static magnetic field and cause a shift of atomic energy levels, which is known as the Zeeman effect. The interaction Hamiltonian of a field $\vec{B}$ with the magnetic moment of the ion $\vec{\mu}$ can be expressed as

$$\hat{H}_0 = -\hat{\vec{\mu}}\vec{B} \tag{5.1}$$

where the magnetic moment of the $^{40}Ca^+$ ion is a combination of the nuclear spin $\hat{\vec{S}}$ and the orbital angular momentum $\hat{\vec{L}}$, with $\hat{\vec{J}} = \hat{\vec{S}} + \hat{\vec{L}}$ and under the condition that the interaction with the magnetic field is small compared to the spin-orbit coupling it follows

$$\hat{\vec{\mu}} = -g\frac{e}{2m_e}\hat{\vec{J}} \tag{5.2}$$

where g is the Landé factor

$$g \approx \frac{3}{2} + \frac{S(S+1) - L(L+1)}{2J(J+1)} \tag{5.3}$$

with spin angular momentum S, orbital angular momentum L and total angular momentum J. The magnetic field is chosen to be aligned in z direction without loss of generality $\vec{B} = (0, 0, B)$ which leads to

$$\hat{H}_0 = g\frac{e}{2m_e}\hat{J}_z B = g\frac{\mu_B}{\hbar}\hat{J}_z B \tag{5.4}$$

where $\mu_B = \frac{e\hbar}{2m_e}$ is the Bohr magneton. The energy eingenvalues are then given by

$$E_{m_j} = g\mu_B m_j B = m_j \hbar \omega_L \tag{5.5}$$

with $J_z = \hbar m_j$ and $m_j = -j, -j+1, ..., j-1, j$. The magnetic sublevels are then split equidistantly by $\hbar\omega_L$, where $\omega_L = g\mu_B B/\hbar$ is the *Lamor frequency*. In the case of our spin qubit, the $4S_{1/2}$ state is split by around $2\pi \times 10\,\mathrm{MHz}$, which is realized by a magnetic field of about $B \approx 0.37\,\mathrm{mT} = 3.7\,\mathrm{G}$. This splitting is chosen as a compromise between being smaller than the natural linewidth of the $S_{1/2} \leftrightarrow P_{1/2}$ cycling transition and being large enough to avoid spectral crowding on the $S_{1/2} \leftrightarrow D_{5/2}$ quadrupole transition, which is essential for spin qubit readout, as described earlier in chapter 2.1. The first approach using permanent magnets was realized by Thomas Ruster [Rus16]. The quantizing magnetic field is generated by 80 Sm_2Co_{17} round magnets with a diameter of 6 mm and a length of 4 mm. This material was chosen because it has a remanence of $> 1\,\mathrm{T}$ in combination with a temperature dependence of about -0.03 %/K, which was the lowest value known to us at that time for common permanent magnet materials. These magnets are arranged in two circular shaped aluminum frames with an outer diameter of 128 mm and an inner diameter of 108 mm, which are attached vertical to the trap axis in a coaxial geometry, each at a distance of 258 mm from the trap center (see Fig. 5.1). The apparatus, composed of the vacuum chamber, laser focusing optics, non evaporative getter pump and the trap rf drive resonater, is surrounded by a three-layer magnetic field shielding enclosure. The inner and outer layers are made out of 2 mm thick μ-metal (80 % Ni and 20 % Fe, relative permeability $\sim$ 80000), where the inner layer is made out of 6 mm thick Al. At the cutting edges, where the box can be opened, overlapping μ-metal lids ensure high shielding efficiency. Attenuation factors were measured to be in the range of 20 to 30 dB for signal frequencies between 50 and 100 kHz. Previously, a similar quantizing magnetic field was generated by coaxial coils and a current of several amperes (typical value 3.36 A). Using the same magnetic shielding enclosure, the coherence times were strongly restricted to $\approx$ 60 ms in a Spin-Echo sequence and $\approx$ 30 ms in a Ramsey sequence. The permanent magnets described above increased the coherence time significantly to $\approx 2.1\,\mathrm{s}$ in a Spin-Echo sequence and $\approx 300\,\mathrm{ms}$ in a Ramsey sequence [Rus16]. Nevertheless, large drifts of the qubit frequency were observed on a large time scale. The following chapter focuses on the quantification of this drift, as well as the determination of the error source and an attempt to enhance the stability based on the assumption that the main source is the residual temperature dependence of the magnets.

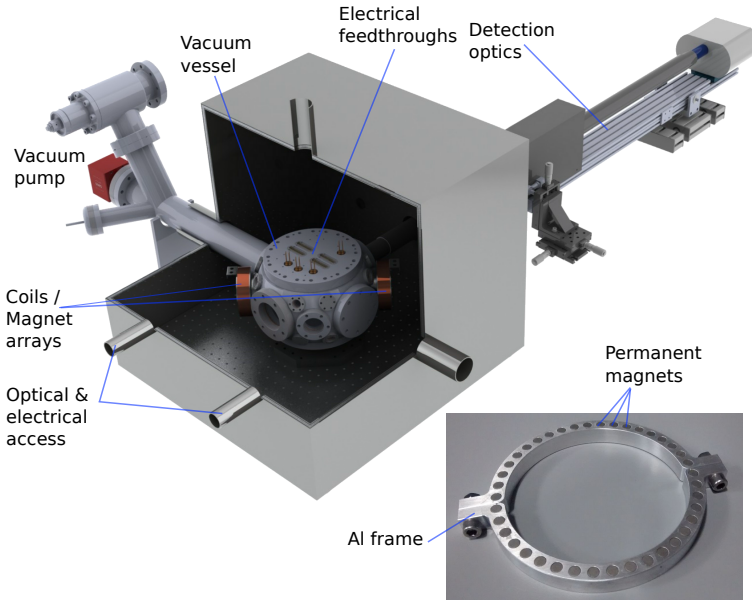

Figure 5.1.: Setup of the vacuum chamber, which contains the ion trap enclosed by a magnetic shielding box made out of μ-metal (80 % Ni and 20 % Fe, permeability ~ 80000). Right lower corner: First design aluminum frame with 40 Sm_2Co_{17} equally spaced permanent magnets. Two of these rings lead to a ground state $S_{1/2}$ Zeeman splitting of around $2\pi \times 10.5\,\mathrm{MHz}$ [Rus16].

5.2. Setup of the Temperature Measuring Device

To confirm the presumption that the observed long-time drifts of the qubit frequency are induced by temperature drifts of the magnets, a temperature logging device is installed on each of the aluminum frames. It automatically saves the temperature in configurable timesteps. Considering the sensitivity of the ion, it is obvious that even small fluctuations in the magnetic field can play a significant role. Considering the RTC of SmCo and earlier long time drift measurements the temperature deviation is expected in the range of 10^{-1} to 10^{-2} K and therefore the temperature has to be recorded with high resolution of 0.01 K. The temperature sensor setup capable of measuring with this precision consists of

- 2 × Temperature Sensor Greisinger GOF 115 Pt
- 2 × Thermometer Greisinger GMH 3750
- NI-USB 6001 (Analog Input)

The high precision thermometer GMH 3750, usually employed for calibration purposes, offers not only the required resolution of 0.01 K but also a high accuracy of ≤ 0.03 K. While the high resolution is required for our purposes, the high accuracy is not important because the main interest lies in the relative temperature deviation. The device provides an analog output of 0 to 1 V, freely scalable in the measuring range of -199 °C to +199 °C, with a 13 bit resolution and an accuracy of 0.05 %. The chosen measurement range is then projected in the analog digital converter on the 13 bits, to provide as much resolution as possible under the technical limitations. The output is chosen to be scaled as 20 °C ≡ 0 V and 30 °C ≡ 1 V, which is large enough to cover temperature fluctuations up to ± 5 °C compared to our standard lab temperature of around 25 °C, while it is small enough to not impede the high resolution. On 13 bit and a temperature range of 10 °C, the temperature can be digitalized in steps of $10/2^{13}$ °C ≈ 0.001 °C. The connected temperature sensor is a four-wire configuration Pt100 precision sensor with a temperature range of -50 to +200 °C. It is a self-adhesive temperature surface sensor and easily attachable to the magnet frames. The DAQ USB Device "NI USB-6001" is used as an analog-to-digital converter, it takes in the two analog outputs of each thermometer in differential mode and communicates this voltage difference to the control computer via USB. With this setup it is now possible to log even very small temperature changes and therefore evaluate the correlation between magnetic field drift and temperature drift.
A typical long time measurement of the qubit resonance frequency is shown in Fig. 5.2. It is easily visible that the temperature drift is a main source for the magnetic field fluctuation and therefore causes the shift of the qubit frequency. The rise in temperature lowers the magnetic field, which leads to a decreasing qubit frequency. Fig. 5.3 shows the deviation of the qubit frequency versus the temperature. The simulation, described in the following section, coincides approximately with the measurement.

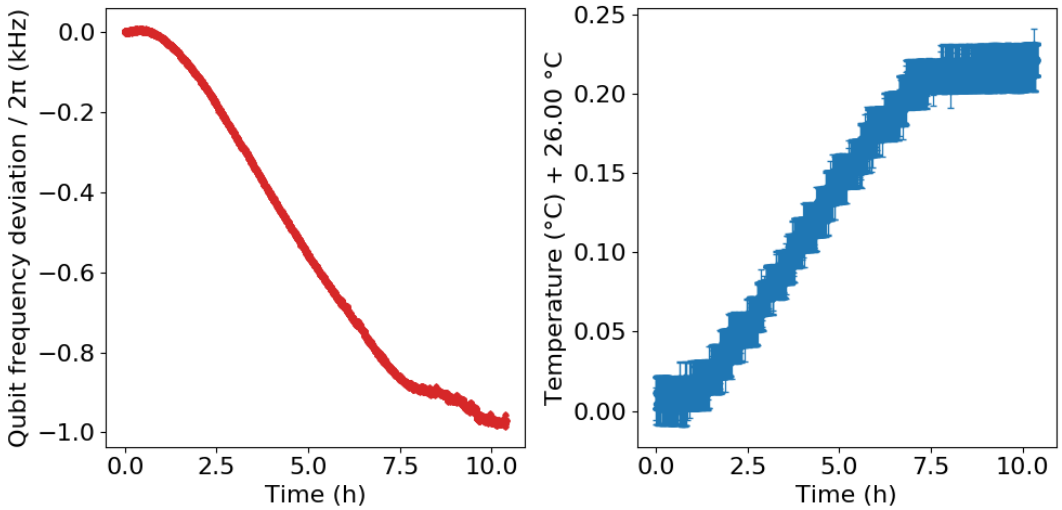

Figure 5.2.: Top: Drift of qubit frequency over a time of $\sim 10\,\mathrm{h}$. Bottom: Temperature drift measured on the aluminum frame of the Sm_2Co_{17} permanent magnets during the same time.

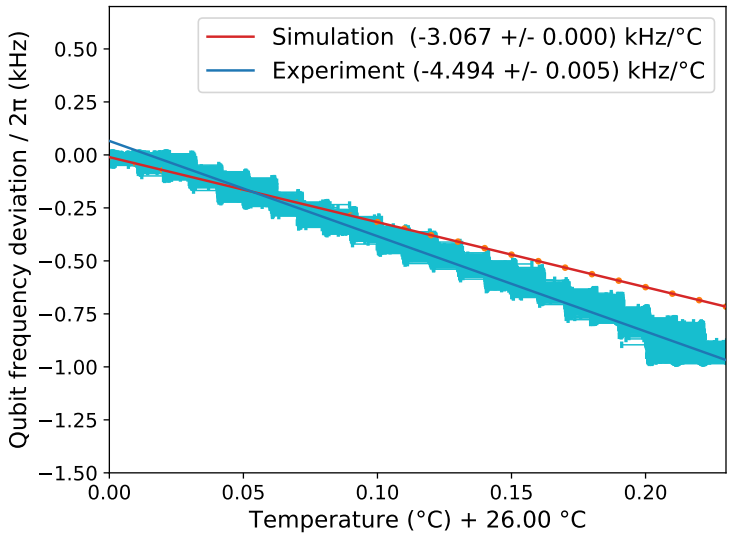

Figure 5.3.: Comparison of the simulation and experimental results of the permanent magnet setup. The data coincides approximately with the simulation, further described in the following chapter 5.3.

5.3. Design and Fabrication of a new Permanent Magnet Setup

There are several possibilities to reduce the instability of the magnetic field. One could actively stabilize the temperature, which is however challenging as the temperature would have to be measured and stabilized on the 10 mK range or even below. We have decided to implement a passive approach to increase the magnetic field stability, for which a new permanent magnet setup has been conceived, manufactured and tested. Here, the new magnet frames are mounted on flanges above and beneath the vacuum vessel, to increase mechanical stability compared to the previous system, see Fig. 5.4. The simulation to find the optimal configuration has been done with *Mathematica*[1]. Each magnet is modeled by a magnetic dipole moment

$$\mu = B_R V/\mu_0 \tag{5.6}$$

with remanence of the magnetic material B_R, magnet volume V and vacuum permeability μ_0. The outer magnetic field at position $\vec{r}$ induced by a dipole located at position $\vec{r}_i$, under the assumption that the distance $|\vec{r}_i - \vec{r}|$ is much larger than the height and diameter of the permanent magnet, is given by

$$\vec{B}_i(\vec{r}, \vec{r}_i) = \frac{\mu_0}{4\pi} \frac{3\vec{r}(\vec{\mu}_i \cdot (\vec{r}_i - \vec{r})) - \vec{\mu} \cdot (\vec{r}_i - \vec{r})^2}{|\vec{r}_i - \vec{r}|^5}. \tag{5.7}$$

The magnetic dipoles sum up to a total field of

$$\vec{B}_{tot}(\vec{r}) = \sum_i \vec{B}_i(\vec{r}, \vec{r}_i). \tag{5.8}$$

The magnets are of cylindrical shape and we assume the dipole moment to be aligned along the cylinder axis. In the previous setup, the 80 Sm_2Co_{17} magnets with a remanence of about 1 T lead to a magnetic field of 0.37 mT at the trap center position. The new setup is supposed to generate a magnetic field of same strength, but with less temperature dependence and higher homogeneity along the trap center. To reduce the reversible temperature coefficient $\mathrm{RTC}_{\mathrm{SmCo}} \approx -0.03\%/\mathrm{K}$ of Sm_2Co_{17}, a second magnetic material NdFeB with a remanence of $B_R \approx 1.2\,\mathrm{T}$ and a reversible temperature coefficient of $\mathrm{RTC}_{\mathrm{NdFeB}} \approx -0.1\,\%/\mathrm{K}$ is used. Close to each samarium cobalt magnet, a smaller neodymium magnet is placed, oriented in opposite direction. Now, the relation between the dimensions of the two magnet types can be chosen that in case of e.g. an increasing temperature the decrease of the field generated by the samarium cobalt magnets is lowered due to a lower counteracting field caused by the neodymium magnets. For one pair of magnets, the magnetic field change δB resulting from a temperature change δT, at a location sufficiently far away from the magnets, is given by

$$\delta B \propto \mathrm{RTC}_{\mathrm{SmCo}} \mu^{(0)}_{\mathrm{SmCo}} \delta T + \mathrm{RTC}_{\mathrm{NdFeB}} \mu^{(0)}_{\mathrm{NdFeB}} \delta T \tag{5.9}$$

[1] Wolfram Mathematica 11, Student Edition

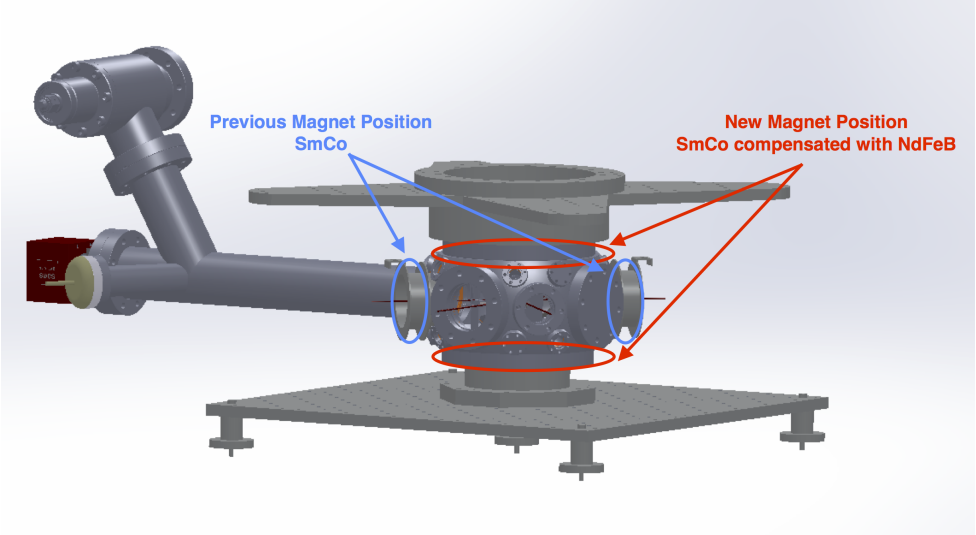

Figure 5.4.: Sketch of the trap setup without enclosure. Blue: Position of the previous magnet frames. Red: Position of the new magnet frames.

where $\mu^{(0)}$ denotes the magnetic dipole moments at a reference temperature. In order to obtain $\delta B = 0$, we set

$$\mathrm{RTC}_{\mathrm{SmCo}}\mu^{(0)}_{\mathrm{SmCo}} + \mathrm{RTC}_{\mathrm{NdFeB}}\mu^{(0)}_{\mathrm{NdFeB}} = 0 \tag{5.10}$$

It follows that

$$\frac{\mathrm{RTC}_{\mathrm{SmCo}}}{\mathrm{RTC}_{\mathrm{NdFeB}}} = -\frac{\mu^{(0)}_{\mathrm{NdFeB}}}{\mu^{(0)}_{\mathrm{SmCo}}} = \frac{V_{\mathrm{NdFeB}}}{V_{\mathrm{SmCo}}} \tag{5.11}$$

which serves for choosing the ratio of the magnet volumes. Note that the minus sign in the equation above cancels with the implicit minus sign of the magnetic dipole moment of the NdFeB magnets arising from their reverse orientation. Fig. 5.5 shows a sketch of the old and new aluminum frames and the position of the magnets. An ideal configuration is realized by using Sm_2Co_{17} magnets of size $\varnothing 8\,\mathrm{mm} \times 5\,\mathrm{mm}$ which are compensated by NdFeB of size $\varnothing 5\,\mathrm{mm} \times 4\,\mathrm{mm}$. Due to the fact that $\varnothing 5\,\mathrm{mm} \times 4\,\mathrm{mm}$ was not available as standard magnet these are implemented by using two $\varnothing 5\,\mathrm{mm} \times 2\,\mathrm{mm}$ NdFeB magnets. Considering about 10 % tolerance in the remanence per magnet, this replacement should have no significant impact.[2] To increase homogeneity, it is advantageous to generate the magnetic field by using a large number of small magnets instead of a few stronger ones. In the new setup, 88 Sm_2Co_{17} and 176 NdFeB magnets are used. The inner radius of the aluminum frames is predetermined by the outer radius of the vacuum vessel flanges to be 101.5 mm. The magnets are centered at a radius of 108 mm, the outer radius of the frames is given by 117 mm. On each semicircular frame the magnets are equally spaced by 8.2 °, the corresponding blueprint with all dimensions can be found in the Appendix A.2.

[2] IBS Magnet, Berlin, Germany

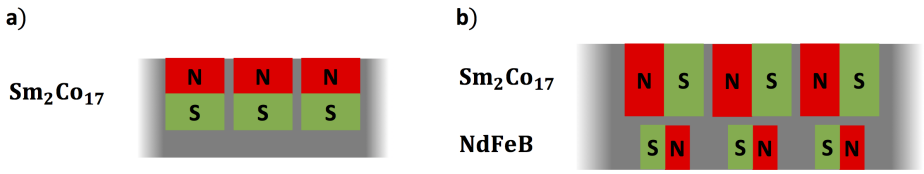

Figure 5.5.: Orientation of the permanent magnets inside the aluminum frame. a) Previous setup where nearby Sm_2Co_{17} magnets of size ∅6 mm × 4 mm are oriented in the same direction. b) New setup with larger Sm_2Co_{17} magnets of size ∅8 mm × 5 mm, which are compensated by NdFeB of size ∅5 mm × 4 mm in a way that the temperature drifts of the different materials ideally cancel each other out.

The magnet frames are made out of aluminum and manufactured in our institutes' workshop.[3] Fig. 5.6 shows one of the magnet frames after the magnets are inserted and glued. The magnets in the two half-rings are oriented in opposite direction, such that the total field direction is aligned along the intersection line.

[3]Institute of Physics, University of Mainz

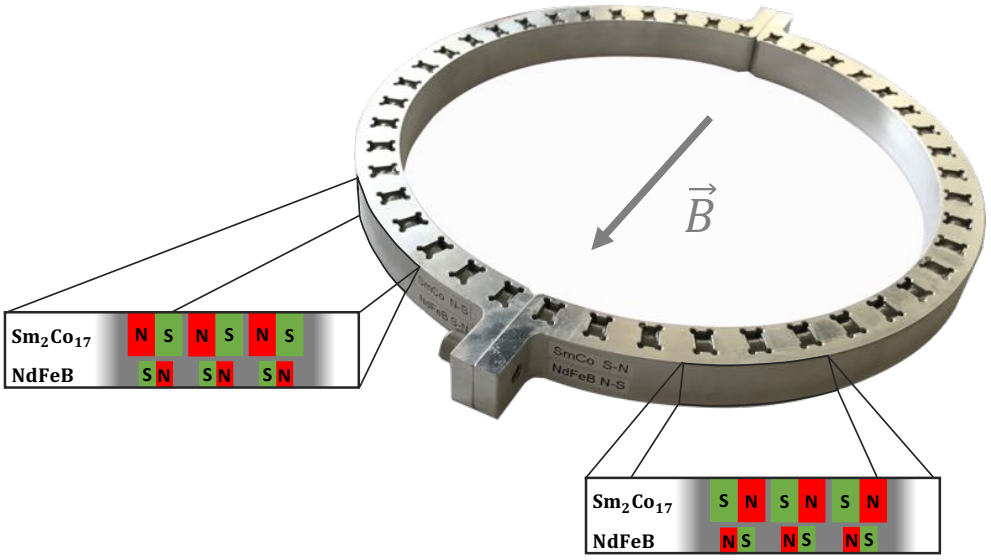

Figure 5.6.: One of the two new aluminum frames providing the quantizing magnetic field. The circular frames are divided into two parts with each 22 Sm_2Co_{17} and 44 NdFeB magnets oriented in opposite direction. This leads to a magnetic field along the intersection line.

5.4. Homogeneity along Trap Axis

The magnetic field along the trap axis is of major importance. As explained in Sec. 2.3, ion shuttling operations are the cornerstone of our approach to realize a scalable system for quantum information. Ions residing at different locations in the trap accumulate a different phase, which has to be taken into account during the computational sequence to correct for them. This leads to more calibration overhead and an additional error source. Simulations of the novel magnetic setup indicate that it could potentially give rise to a substantially increased magnetic field homogeneity along the trap axis.
Fig. 5.7 shows the simulated qubit frequency deviation with respect to the trap center of the previous and the new permanent magnet setup. For the new setup, the maximum deviation of the qubit frequency should be reduced by a factor of five.

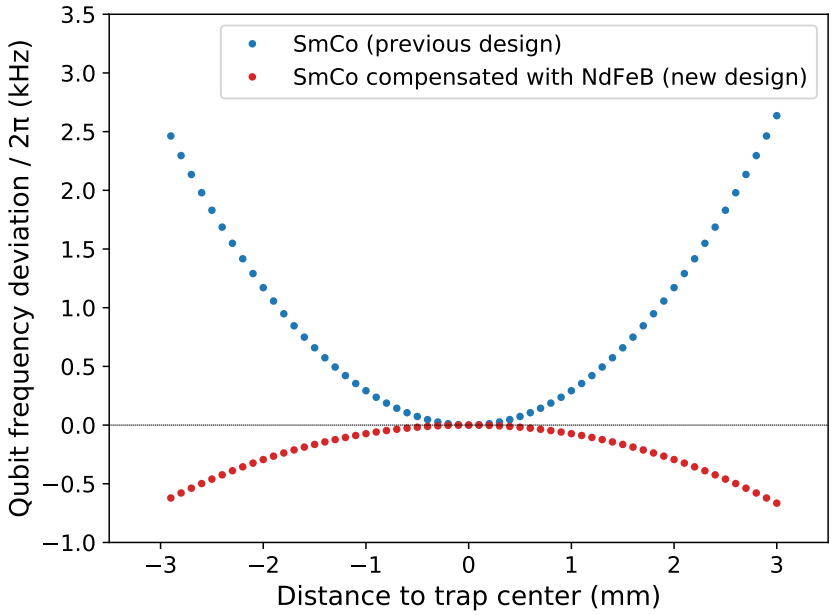

Figure 5.7.: Simulated homogeneity along the trap axis.

Experimentally, the phase accumulation is measured with the following scheme [Rus17a]: First, two ions are trapped in the laser interaction zone, referred to as the reference and the probe ion. The two-ion crystal is Doppler cooled on the $S_{1/2} \leftrightarrow P_{1/2}$ cycling transition, followed by resolved sideband cooling on the stimulated Raman transition to achieve a state close to the motional ground state. Frequency selective pumping on the $S_{1/2} \leftrightarrow D_{5/2}$ quadrupole transition is used to initialize to the $|\uparrow\uparrow\rangle$ state. An entangling gate operation generates a Bell state $(|\uparrow\uparrow\rangle + |\downarrow\downarrow\rangle)/\sqrt{2}$, from which the *sensor state* $(|\uparrow\downarrow\rangle + |\downarrow\uparrow\rangle)/\sqrt{2}$ is generated by means of an additional $\pi/2$ rotation on the two ions. The two-ion crystal is now separated by applying time-dependent dc voltages on the trap electrodes, as described in section 4.6, and transported to the

reference and probe locations x_1 and x_2. During an interrogation time T, the ions accumulate a phase $\varphi(x_1, x_2, T)$, which leads to the state $\left(|\uparrow\downarrow\rangle + e^{i\varphi}\,|\downarrow\uparrow\rangle\right)/\sqrt{2}$. Both ions are now individually moved back to the laser interaction zone to perform spin readout. The dc magnetic field difference between the ion locations is determined by the phase accumulation rate via

$$\dot{\varphi} \equiv \Delta\omega(x_1, x_2)_{dc} = \frac{g\mu_B}{\hbar}\Delta B(x_1, x_2) \tag{5.12}$$

During the interrogation time, the reference ion is always placed at segment 1, while the probe ion is successively placed at segments 3 to 32. For each distance, the optimal interrogation time T and the frequency deviation $\Delta\omega$ is determined via a Bayesian frequency estimation. These technique is based on a *Bayesian experiment design* algorithm [Mac14][Wie16] and was implemented by Thomas Ruster, further details can be found in [Rus17b].

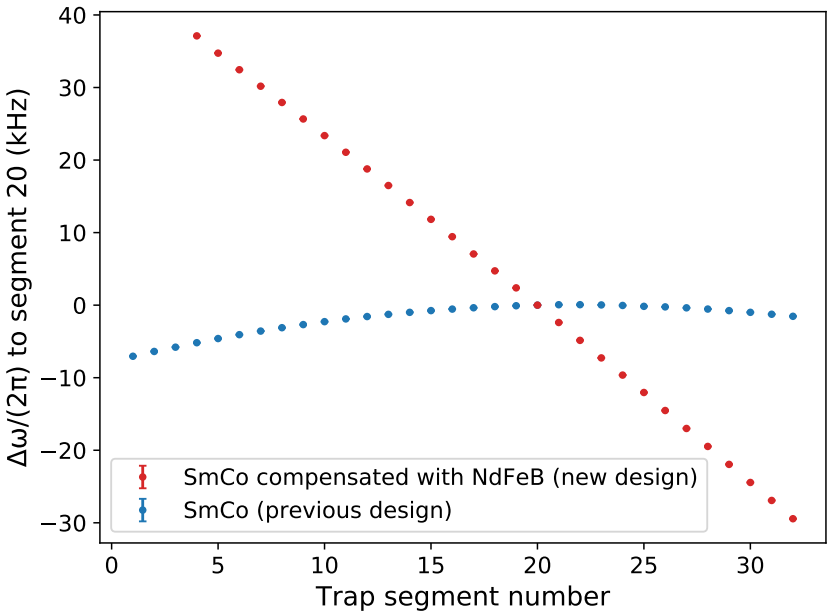

Figure 5.8.: Experimental result of the homogeneity along the trap axis.

In Fig. 5.8, the result of the measurement described above is shown, comparing the magnetic field map of the previous and the new setup. In the previous setup, the absolute inhomogeneity is about a factor 3.5 larger than expected, but the overall curve is similar and the extremum is close to the trap center. It had been shifted closer to the laser interaction zone at segment 20 by adding eight additional Sm_2Co_{17} magnets at the outside of one aluminum frame. While this bears some degree of similarity with the simulation result, the magnetic field map of the new setup does not match the simulation result. A difference in the qubit frequency between the trap segment 16 and the first segment (distance of 200 μm $\times$ 15 segments = 3 mm) of less

than $2\pi\times 1\,\mathrm{kHz}$ was expected, whereas the real deviation of $2\pi\times$ 38.88 kHz is about 40 times higher. This indicates that the field extremum is shifted far away from the trap center. The first assumption that this effect might be caused by an external field far away of the trap could not be confirmed. After closing the μ-metal shielding box, the inhomogeneity did not change significantly. The vacuum chamber itself is made out of non-magnetizable steel and no changes were made compared to the prior magnetic setup, so this can not be the reason of the inhomogeneity. Compared to the old setup with a ring diameter of the magnetic frames are of much larger size and thus the deviation between the ideal and actually geometry might be larger as well. Another possible source impeding the magnetic field are the screws, which tighten the aluminum frames on the flanges of the vacuum chamber. These screws are standard steel screws and therefore magnetizable. When opening the enclosure box again, these could be exchanged by non-magnetizable screws to exclude this as an error source.

5.5. Coherence Time Measurements

The main decoherence source for the $^{40}Ca^{+}$ spin qubit is given by magnetic field fluctuations. Therefore, the measurement of the coherence time provides an insight in the magnetic field stability. The qubit coherence is characterized via Ramsey-type measurements. The measurements are performed on a Doppler-cooled single ion, initialized in $|\uparrow\rangle$. A coherent $\pi/2$-pulse on the stimulated Raman transition transfers the qubit into the superposition state $(|\uparrow\rangle + |\downarrow\rangle)/\sqrt{2}$. During the wait time τ, a phase φ is accumulated, leading to the state $\left(|\uparrow\rangle + e^{i\varphi}|\downarrow\rangle\right)/\sqrt{2}$. For a single execution of the sequence, the accumulated phase is given by

$$\varphi = \frac{g\mu_B}{\hbar}\int_0^\tau \Delta B(t)dt \tag{5.13}$$

where $\Delta B(t)$ is the time-dependent deviation of the magnetic field to the one which corresponds to the currently set qubit frequency. In case of a wrongly set frequency, but without fluctuations, each repetition of the measurement sequence would lead to the same phase. While a direct measurement of φ is not possible, the sequence is repeated in order to statistically estimate φ. Due to the random nature of the fluctuations, φ is a random variable. The state of the qubit is a statistical mixture and the corresponding density matrix can be written as

$$\hat{\rho} = \frac{1}{2}\begin{pmatrix} 1 & Ce^{-i\varphi} \\ Ce^{i\varphi} & 1 \end{pmatrix} \tag{5.14}$$

with contrast $C = 2|\rho_{12}|$, describing the randomization of the phase φ.
The resonant laser near 397 nm, directed at segment 20, does not switch off perfectly, which can lead to residual photon scattering. Therefore, the ion is moved out of the laser interaction zone during the wait time. For the measurements discussed in the following, the ion is transported to segment 21, 200 μm away from the laser interaction zone. After the return transport, a second $\pi/2$ pulse is applied, either including a $\pi/2$

phase with respect to the first pulse to accomplish a qubit readout in the Y basis, or without additional phase for readout in the X basis. The probabilities to detect the qubit in the $|\uparrow\rangle$ state are then given by

$$p_x = \frac{1}{2}\left(1 - C\cos\varphi\right) \tag{5.15}$$

$$p_y = \frac{1}{2}\left(1 + C\sin\varphi\right) \tag{5.16}$$

It therefore follows

$$C = 2\sqrt{\left(p_x - 1/2\right)^2 + \left(p_y - 1/2\right)^2} \tag{5.17}$$

Measuring each basis X and Y N times with the result of n_x and n_y times $|\uparrow\rangle$, the probabilities p_x, p_y are estimated by

$$p_x = \frac{n_x}{N}; \qquad\qquad p_y = \frac{n_y}{N} \tag{5.18}$$

The coherence and phase can then be estimated using the maximum likelihood method [Rus16]. Fig. 5.9 shows the Ramsey measurement schematically. To avoid residual spurious phase randomization from field oscillations at the 50 Hz AC-line frequency, the beginning of each measurement is synchronized with the AC-line.

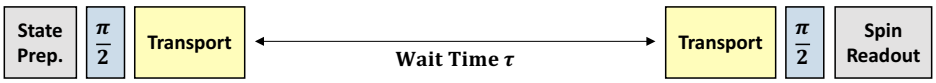

Figure 5.9.: Ramsey measurement scheme.

Fig.5.10 shows the measured Ramsey contrast. The fit function has been selected under the assumption that the fluctuations causing the decoherence are stationary, Gaussian and static, i.e. they feature correlation times longer than the phase accumulation times τ [Mon11]. This leads to a Gaussian decay of the contrast:

$$C(\tau) = e^{-\frac{\tau^2}{2\tau_d^{*2}}} \tag{5.19}$$

The coherence time τ_d^* is given by

$$\frac{1}{\tau_d^*} = \frac{g\mu_B}{\hbar}\sqrt{\langle \Delta B \rangle} \tag{5.20}$$

i.e. it is inversely proportional to the rms shot-to-shot deviation of the magnetic field. The fit of the Ramsey data yields a dephasing time constant of $\tau_d^* = 238(9)\,\mathrm{ms}$. This result is close to the previously achieved dephasing time constants using the old

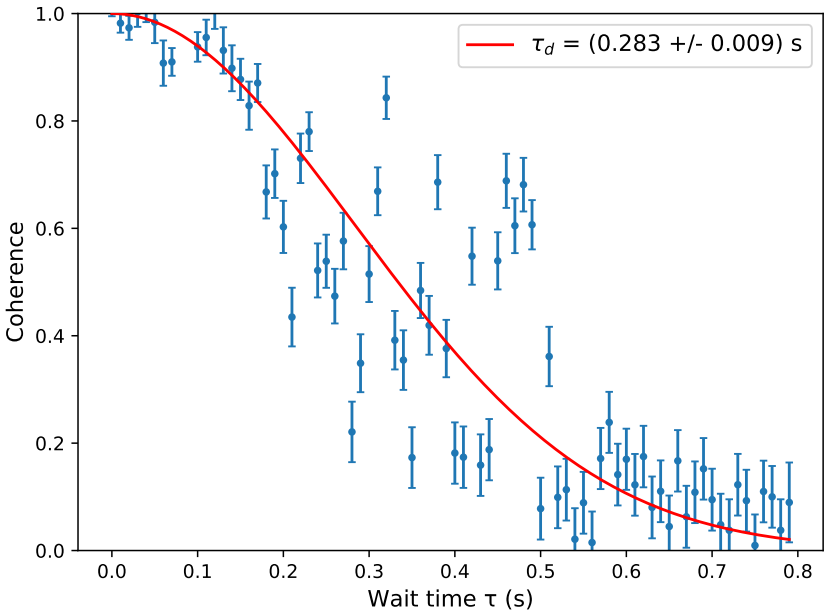

Figure 5.10.: Ramsey measurement with the new permanent magnet setup. Qubit coherence versus wait time τ. Each data point results out of 300 repetitions of the Ramsey scheme, including a readout of the σ_x and σ_y operator.

magnet configuration of $\tau_d^* = 300(50)\,\mathrm{ms}$ [Rus16]. Noticeable are large fluctuations for wait times $> 0.15\,\mathrm{s}$. These fluctuations are most likely caused by non-stationary noise, which means the mean value of the noise does change over time and differs in each measurement. To suppress fluctuations on a timescale lower than the wait time we employ a Spin-Echo scheme, where an additional rephasing π-pulse after half of the wait time can be added. The Spin-Echo sequence is represented in Fig. 5.11. The corresponding measurement and fit in Fig. 5.12 shows that by taking advantage of this rephasing pulse a much longer dephasing time constant of $\tau_d = 1.13(3)\,\mathrm{s}$ is obtained.

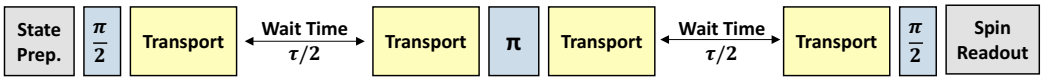

Figure 5.11.: Spin-Echo measurement scheme.

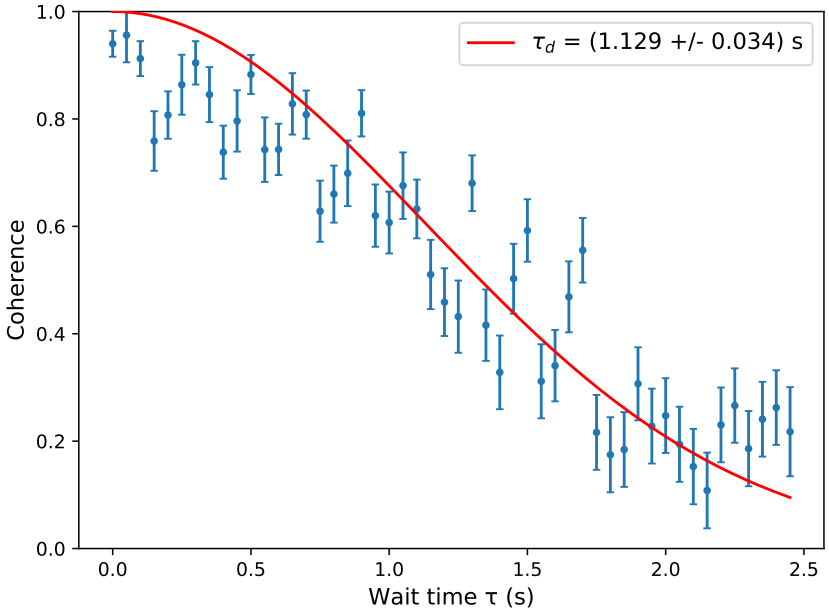

Figure 5.12.: Spin-Echo measurement with the new permanent magnet setup. Qubit coherence versus wait time τ. Each data point results out of 300 repetitions of the Spin-Echo scheme, including a readout of the σ_x and σ_y operator.

5.6. Qubit Frequency Drift compared to Temperature Drift

The main motivation behind the new permanent magnet setup is the reduction of temperature drifts of the qubit frequency. In this section, we derive the expected residual drift from simulations and compare it to measurement data.

The simulation of the temperature dependence of the magnetic field at the trap is shown in Fig. 5.13. It is based on the assumption that the reversible temperature coefficient (RTC) of the Sm_2Co_{17} magnets is $\mathrm{RTC_{SmCo}} = -0.03\,\%/°\mathrm{C}$ and $\mathrm{RTC_{NdFeB}} = -0.1\,\%/°\mathrm{C}$ for the NdFeB magnets [4].
Within a linear expansion around the operating temperature T_0, the magnetic field magnitude at a given location is given by

$$\Delta B(T) = B(T_0)\frac{\mathrm{RTC}\cdot\Delta T}{100} \tag{5.21}$$

Where $B(T)$ is the temperature dependent magnitude of the total magnetic field at this location in Eq. (5.8). For the combination of SmCo and NdFeB in this particular

[4] IBS Magnet, Berlin, Germany

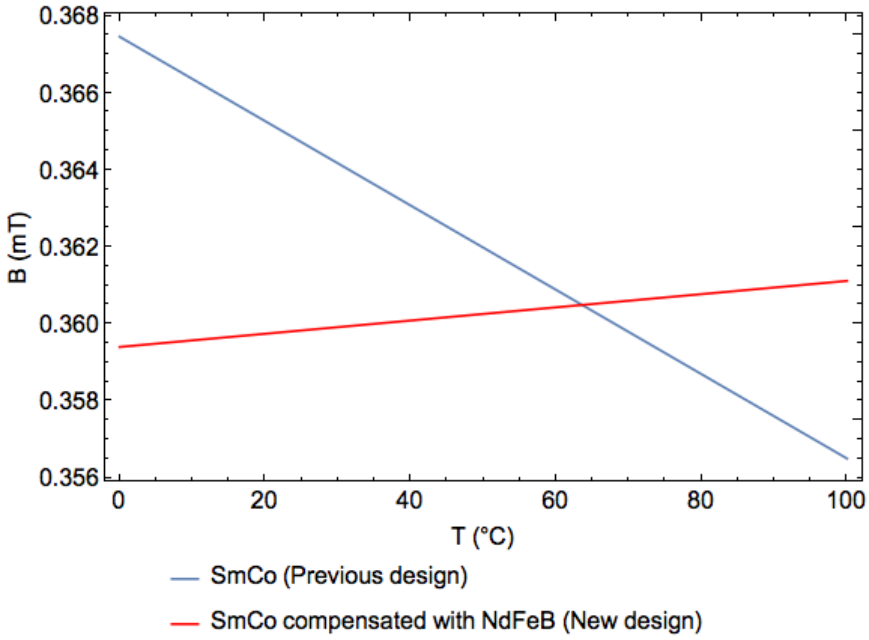

Figure 5.13.: Simulation of the magnetic field generated at the trap center by the permanent magnets according to the temperature. The dependence of the new magnets on the temperature (red) is with 0.0047 %/°C much lower than the previous one -0.03 %/°C (blue).

case the two magnetic fields sum up to

$$\Delta B(T) = (B_{\mathrm{SmCo}}(T_0)\mathrm{RTC}_{\mathrm{SmCo}} - B_{\mathrm{NdFeB}}(T_0)\mathrm{RTC}_{\mathrm{NdFeB}})\,\frac{\Delta T}{100} \tag{5.22}$$

The resulting reversible temperature coefficient in our simulation can be adjusted by the relation of $B_{\mathrm{SmCo}}(T_0)$ to $B_{\mathrm{NdFeB}}(T_0)$ at any given temperature T_0. Ideally the RTCs completely cancel out at $B_{\mathrm{SmCo}}(T_0)/B_{\mathrm{NdFeB}}(T_0) = \mathrm{RTC}_{\mathrm{NdFeB}}/\mathrm{RTC}_{\mathrm{SmCo}}$. Considering the restraints according to magnet size and available space in the setup, which is a maximum height of 22 mm for the aluminium frames, the simulation results in a combined temperature coefficient of

$$\mathrm{RTC} = \frac{B_{\mathrm{SmCo}}(T_0)\mathrm{RTC}_{\mathrm{SmCo}} - B_{\mathrm{NdFeB}}(T_0)\mathrm{RTC}_{\mathrm{NdFeB}}}{B_{\mathrm{SmCo}}(T_0) - B_{\mathrm{NdFeB}}(T_0)} = 0.0047\,\%/^{\circ}\mathrm{C} \tag{5.23}$$

After mounting the new magnet frames on the vacuum vessel flanges and closing the μ-metal shielding box, the largest temperature drift is expected. The rise in temperature is caused by heat dissipation of the Ca oven inside the box and the electronic devices which are placed close to the box. To quantify the qubit frequency drift over a duration of several hours, the Ramsey measurement sequence (further details in section 5.5) with a wait time of 15 ms is constantly repeated. Meanwhile, the temperature is logged, which enables the analysis of the correlation of qubit frequency

and temperature. Fig. 5.14 and Fig. 5.15 show one of the drift measurements using the new magnetic field configuration. While the first one shows qubit frequency and temperature drift according to the elapsed time, the second one directly shows the relation of both values at the same time. It is clearly visible that the dependence has a linear behaviour. Hence every plot of this kind contains a linear fit of the form $f(T) = f(0) + m \cdot T$.

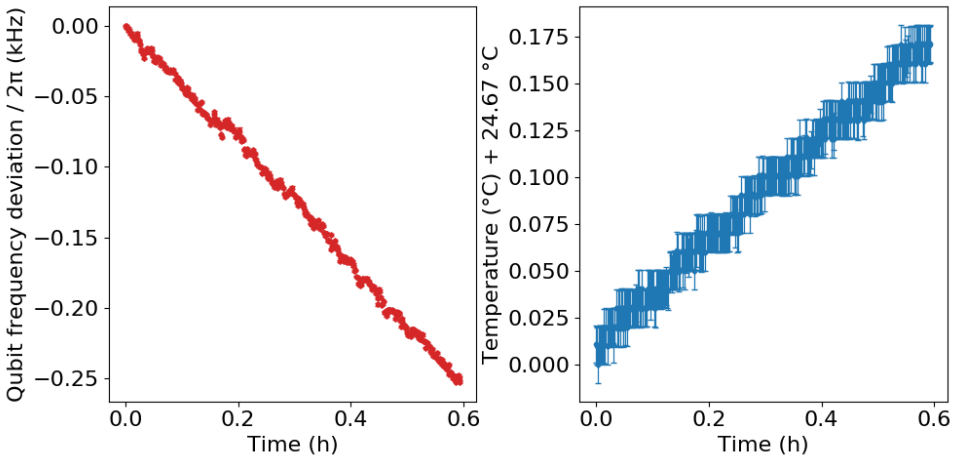

Figure 5.14.: Drift measurement using Sm_2Co_{17} compensated with NdFeB magnets. Top: Deviation of the spin qubit resonance frequency over time. Bottom: Surface temperature measured on the aluminum frame containing the magnets over time.

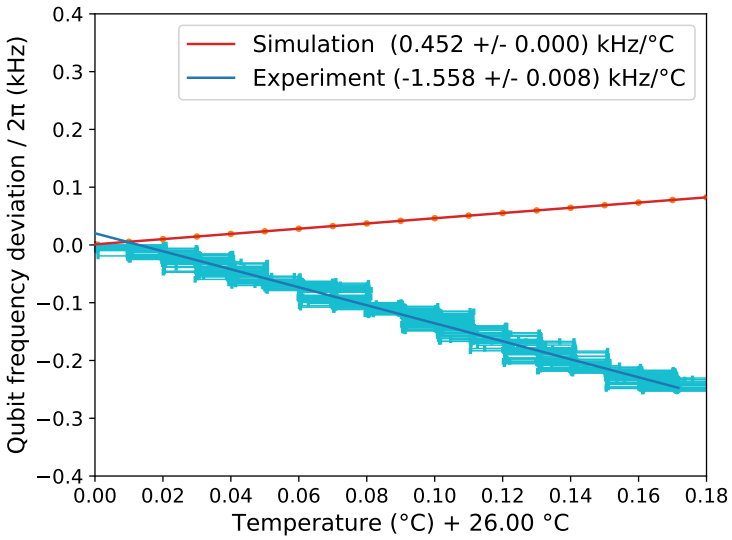

Figure 5.15.: Comparison of the simulation and experimental results of the new permanent magnet setup. It can be seen that the actual temperature coefficient has a reversed sign as compared to the simulation result, and its magnitude is three times larger than expected.

To improve the magnetic field stability further, we identified heat sources close to the μ-metal shielding box and minimized their influence on the magnet temperature inside the box. In particular, we found that the synthesizer generating the trap drive radio frequency signal and a connected oscilloscope were placed in a way that exhaust heat of both devices was directed to the metal box. We have repositioned these devices and conducted further long-time magnetic field drift measurements. In combination with the lower RTC this leads to a much lower absolute frequency deviation, as can be seen in the long time drift measurement over more than 8 h shown in Fig.5.16 and Fig.5.17. Both measures combined therefore lead to a *tenfold* reduction of the qubit frequency drift during an 8 h observation time: The maximum deviation was determined to be 0.995 kHz for a maximum temperature deviation of 0.23 °C for the old setup. The recent measurement for the new setup revealed a maximum qubit frequency deviation of 0.098 kHz for a total temperature deviation of 0.04 °C. However, the reasons for the mismatch between expected and observed RTC currently remain unclear. One notes that the discrepancy in qubit frequency temperature dependence of roughly 1.6 kHz/°C observed for the old setup is similar to the discrepancy of 2.0 kHz/°C for the new one. Therefore, it is possible that the RTC cancellation works, such that the residual temperature dependence is not given by the temperature dependence of the magnets themselves, but rather by thermal expansion/contraction of the aluminum bearings and/or the vacuum vessel. The obtained tenfold reduction in total drift over a typical measurement time is a very promising result, which will facilitate upcoming experiments.

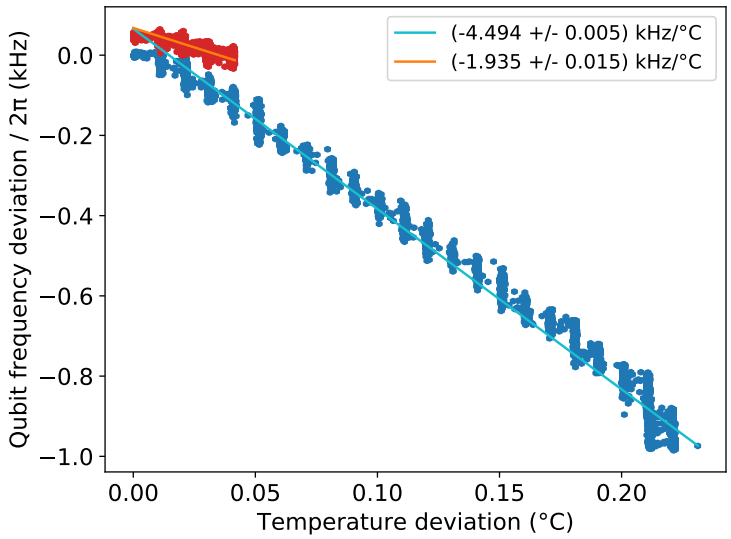

Figure 5.16.: Comparison Long Time Drift $> 8\,\mathrm{h}$. Qubit frequency versus temperature deviation. Marked in blue measurement with the Sm_2Co_{17} magnets, the qubit frequency changes by -4.494(5) kHz/°C. Marked in red the corresponding long time measurement of the new Sm_2Co_{17} magnets compensated with NdFeB. The qubit frequency deviation is suppressed to -1.94(2) kHz/°C, while the absolute temperature drift could also be reduced.

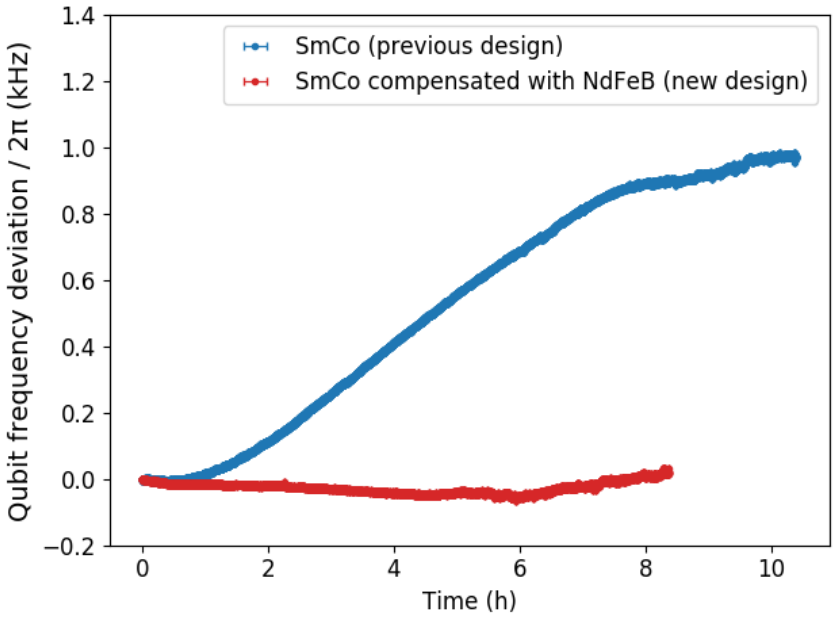

Figure 5.17.: Comparison Long Time Drift $> 8\,\mathrm{h}$. Marked in blue measurement with the Sm_2Co_{17} magnets. Marked in red the corresponding long time measurement of the new Sm_2Co_{17} magnets compensated with NdFeB. The absolute frequency deviation is about ten times lower than in the previous setup.

Chapter 6

Single Qubit Randomized Benchmarking

One of the widespread popular quantum verification and validation protocols to characterize quantum gates is randomized benchmarking (RB), originally proposed by [Kni08]. In this approach, a random gate sequence out of a given set of operations is implemented. A final rotation is chosen which rotates the qubit(s) into the computational basis, such that the ideal outcome of a measurement in this basis is known, and gives either zero or unit probability to detect the qubit e.g. in $|\uparrow\rangle$. After performing the measurement N times, the "survival probability" is estimated out of the number n_c of measurement results that are equal to the expectation as $p = n_c/N$. Averaging over various randomly chosen sequences and especially the decrease of the expectation value $< p >$ with increasing sequence length allows to estimate the gate fidelity. The set of operations is chosen to be the 24 computational gates of the Clifford group proposed in [Bal16a]. To perform large scale fault tolerant quantum computing, an error per single-qubit gate below 10^{-4} is desired [Kni08]. Recently it has been demonstrated by Henning Kaufmann that our setup is capable of performing single-qubit gates with an average error per computational gate of $5.1(2) \cdot 10^{-5}$ [Kau17c], which is well below this limit. In the underlying experiment, a single-qubit is Doppler cooled and initialized in the $|\uparrow\rangle$ state via optical pumping. Then single-qubit gates of the Clifford group are performed using the co-propagating Raman laser beams R1 and CC, in order not to couple to the motional state of the qubit (see Sec. 3.3). We stabilize for small absolute magnetic field drifts by measuring the qubit frequency in a Ramsey experiment after every detection sequence. After the N repetitions of the RB sequence, there are N frequency measurements as well and the correction is done according to the average frequency drift. The tracking itself is shot-noise limited, which leads to effective magnetic field noise even in the case of zero drift.
While executing quantum algorithms, most of the qubits will be subject to idle time. During such idle time, magnetic field drifts lead to undesired accumulation of random phases. In [Kau17c], RB with four qubits is performed. Therefore, the four qubits are stored separately and alternately transported to the LIZ for every gate. Out of technical reasons, this shuttling operation was quite slow and the time in between two gates on the same qubit was 1.57 ms. Due to the very high fidelity measured in the single ion RB and the investigation, that the gates are not sensitive to shuttling induced motional excitation, we assume that the main error source is the phase accumulation

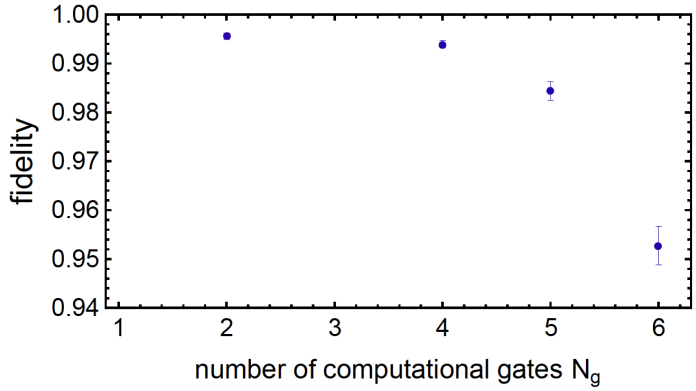

Figure 6.1.: Single-qubit randomized benchmarking on a static ion with an artificial idle time of 1.57 ms after each computational gate. This measurement was taken as a reference to investigate the gate error in the four qubit experiment. The fidelity is a mean fidelity, each data point is based on more than 11000 single measurements. Each sequence is repeated $N = 500$ times and the mean fidelity presented here is the combination of at least 22 RB measurements per N_g. Taken from [Kau17c] (Fig. 8.5).

between the gates. Fig. 6.1 (taken from [Kau17c], Fig. 8.5), shows a single-qubit randomized benchmarking on a static ion with an artificial idle time of 1.57 ms. In the case of $J \equiv N_g = 6$ the idle time for each qubit sums up to $5 \times 1.57\,\text{ms} = 7.85\,\text{ms}$. The result does not coincide with any error model in table 6.1. The following part of this thesis is devoted to the further investigation of the dependence of the fidelity on the spurious phase accumulation for a single ion. We also show how the improved stability of the magnetic field affects these results.

6.1. Randomized Benchmarking Theory

The implementation of single-qubit RB is based on measurements of the fidelity of operations composed of random sequences of Clifford gates. The theory of randomized benchmarking and possible error sources presented in the following follow the description in [Bal16a]. For a sequence of length J, the net operation can be written as

$$S_{\boldsymbol{\eta}} \equiv \prod_{j=1}^{J} \hat{C}_{\eta_j} \tag{6.1}$$

with Clifford operators $\hat{C}_{\eta_j}$ of table III in [Bal16a] indexed by the sequence $\boldsymbol{\eta} = (\eta_1, \eta_2, ..., \eta_J)$, with the η_j being random variables uniformly sampled from the set {1,2,...24}. For modeling the spurious phase accumulation, the sequence of operations

can be extended with unitaries of dephasing rotations $U_j \equiv \exp(-i\delta_j \hat{Z})$ with Pauli $\hat{Z}$ as

$$\tilde{S}_{\boldsymbol{\eta},\boldsymbol{\delta}} \equiv U_1 \hat{C}_{\eta_1} U_2 \hat{C}_{\eta_2} ... U_J \hat{C}_{\eta_J} \tag{6.2}$$

Three different noise models can be distinguished according to the temporal noise correlations

Markovian process
: The errors are Gaussian-distributed with zero mean and variance σ^2 and completely uncorrelated $\delta_j \sim \mathcal{N}(0, \sigma^2)$.

DC process
: $\delta_j = \delta$ is constant during the execution of one sequence, however with respect to different instances, $\delta \sim \mathcal{N}(0, \sigma^2)$ is also a Gaussian random variable with zero mean.

Block-correlated process
: The elements of δ are identical during a time interval of k gates in one sequence $S_{\boldsymbol{\eta}}$. This means the error is constant over blocks or subsequences of a fixed length $M \leq J$. The Markovian limit can be derived from this with the assumption $M = 1$, as well as the DC limit with $M = J$.

For a given sequence η, the measurement is repeated N times, to estimate the fidelity $F_\eta \approx n_c^{(\eta)}/N$ out of the number of results, which matches the expectation $n_c^{(\eta)}$. Thereby, the average is taken over different noise-realizations, e.g. different δ in the DC error model. This measurement is repeated for different sequences η_i, which results in a series of fidelities F_i, following a probability density function (PDF). It is shown in [Bal16a], that for all the above mentioned error models, the PDF of the noise-averaged fidelity $\langle F \rangle$ can be represented by a Γ distribution. The noise-averaged fidelity distribution is then given by

$$f_{\langle \mathcal{F} \rangle}(F) \equiv \nu(F)^{\alpha-1} e^{-\nu(F)/\beta} \beta^{-\alpha} / \Gamma(\alpha) \tag{6.3}$$

The parameters according to the different error models are represented in table 6.1. Histograms of the measured fidelities allow the extraction of the fit parameters $\alpha, \beta, \nu(F)$ and the comparison with the error models in table 6.1. Out of this, the characteristics of the noise can be concluded, which allows the identification of the predominant source and its mitigation.

	Markovian	DC	Block-correlated
α	$\frac{3}{2}n$	$\frac{3}{2}$	$\frac{3}{2}J/(M-1)$
β	$\frac{2}{3}J\sigma^2/n$	$\frac{2}{3}J\sigma^2$	$\frac{2}{3}(M-1)\sigma^2$
$\nu(F)$	$1-F+\frac{2}{3}J^2\sigma^4$	$1-F$	$1-F$
Expectation $\mathbb{E}$	$1-J\sigma^2+\frac{2}{3}J^2\sigma^4$	$1-J\sigma^2$	$1-J\sigma^2$
Mode $\mathbb{M}$	$1-J\sigma^2\left(1-\frac{2}{3n}\right)+\frac{2}{3}J^2\sigma^4$	$1-\frac{1}{3}J\sigma^2$	$1-J\sigma^2\left(1-\frac{2}{3}\frac{M-1}{J}\right)$
Variance $\mathbb{V}$	$\frac{2}{3}J^2\sigma^4/n$	$\frac{2}{3}J^2\sigma^4$	$\frac{2}{3}J(M-1)\sigma^4$
Skew $\mathbb{S}$	$-2\sqrt{2/3n}$	$-2\sqrt{2/3}$	$-2\sqrt{2(M-1)/3J}$

Table 6.1.: Scale and Shape parameters for the corresponding Γ distribution and moments for noise-averaged fidelity distribution $f_{\langle\mathcal{F}\rangle}(F)$ (Eq. 6.3). Taken from [Bal16a].

6.2. Single Qubit RB including Idle Time

The single-qubit randomized benchmarking is performed as described above with a number of computational gates $J = 10$ for variable idle time, which is added after each gate. The 24 Clifford gates are composed of the following gate operations: the identity I, where no operation is performed, the rotation about Z, with an angle of π or $\pi/2$, realized trough adapting the phases of the following X or Y rotation accordingly and the rotation about $X(Y)$. This is realized by a qubit rotation on a stimulated Raman transition, using the copropagating configuration of R1 and CC (see Sec. 3.3). The rotation angles are $\pi/2$ or π, without phase (X) or with 90° phase (Y). The pulse area is calibrated with sufficient precision, such that errors from over- or underrotations are significantly smaller than the effects from spurious Z rotations between the gates. It is of major importance to calibrate the π-pulse time precisely. Therefore, 20 π-pulses are executed for calibration and the 1/20 of the time of the 20th minimum is chosen. The identity operator $\pm I$ is implemented by applying no laser pulse, as well as the $\pm\sigma_z$ operator which just adds a phase to the next gate. Every sequence is executed $n = 100$ times. For the previous magnet system 300 different sequences were measured in total, for the new magnet setup 200 sequences in total. To provide long time drifts to falsify the performance of different sequences we have chosen to perform the measuring flow maximally random. For each sequence ten different idle times are measured. The sequences are measured in blocks of 50, while inside such a block the order of sequence and wait time is randomly chosen. As can be seen in Fig. 6.2 the new permanent magnet setup with less temperature sensitive magnets yields a higher mean survival probability compared to the previous magnet setup. Figure 6.4 shows histograms for the wait times 0.4 ms, 0.8 ms, 1.4 ms and 2.0 ms.

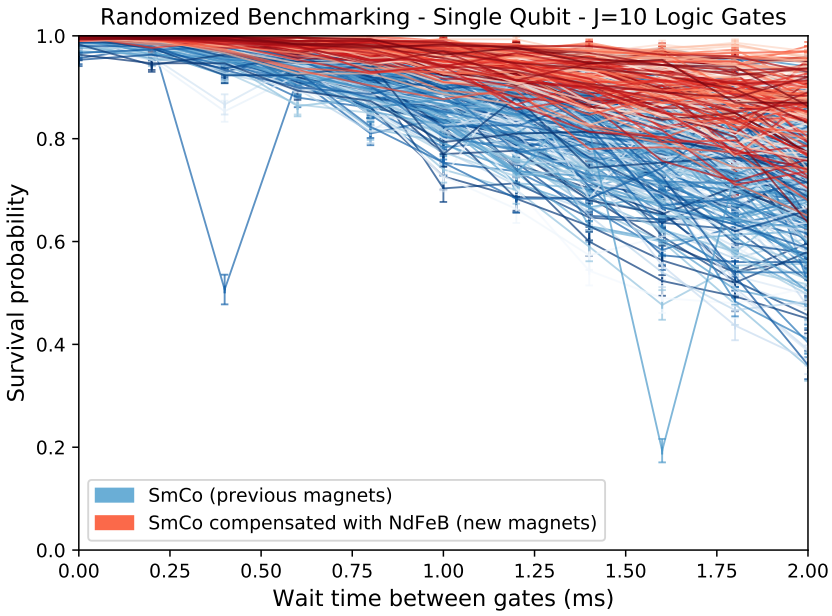

Figure 6.2.: Survival probability detected after performing 10 computational gates for different wait times between the gates. Each line corresponds to a different randomly chosen sequence of Clifford gates. Blue: Data taken by using the magnet setup with SmCo, 300 sequences in total. Red: Data taken by using the new magnet setup with SmCo and NdFeB, 200 sequences in total. Each sequence has length $J = 10$ random gates and is repeated $n = 100$ times.

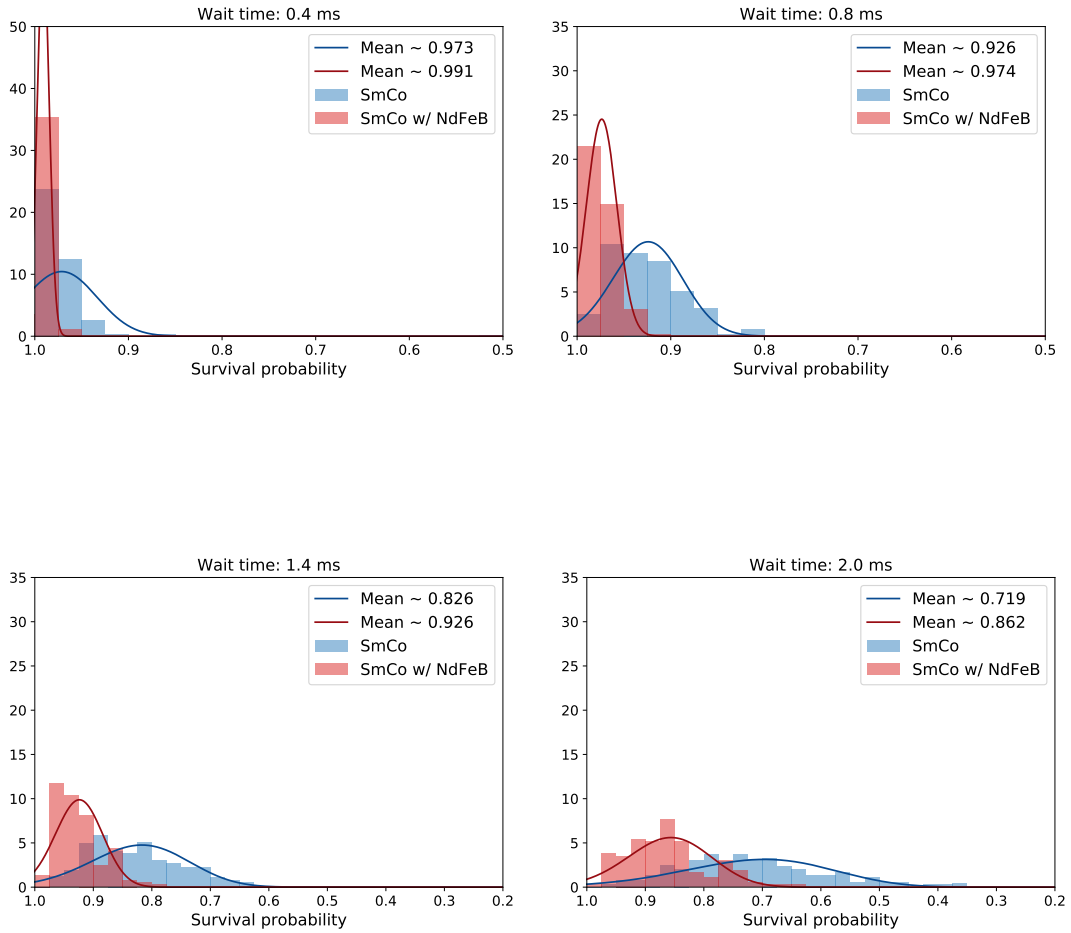

Figure 6.3.: Histogram of the survival probability distribution 10 logic gates at a wait time between every gate of 0.4 ms, 0.8 ms, 1.4 ms and 2.0 ms. Blue: Data taken by using the magnet setup with SmCo, 300 sequences in total. Red: Data taken by using the new magnet setup with SmCo and NdFeB, 200 sequences in total. Each sequence has length $J = 10$ random gates and is repeated $n = 100$ times. The fit function used here is equation 6.3, corresponding values can be found in table 6.2.

The distributions are fitted with equation 6.3 and the result can be found in table 6.2. Fig. 6.4 shows, as an example, the data and fit for an idle time of 0.8 ms after every gate. For this specific time, the a mean fidelity of ~ 0.974 could be achieved with the new setup, which is an enhancement compared to the mean fidelity of ~ 0.926 while using the first permanent magnets. In the present measurements the mean fidelity could be increased for short wait times and decreases slower with increasing wait time. This result is consistent with the presumption that the shift of the magnetic field is a main decoherence source. As demonstrated in section 5.6, the absolute drift of the magnetic field sensitive qubit frequency is reduced and the fidelity is enhanced.

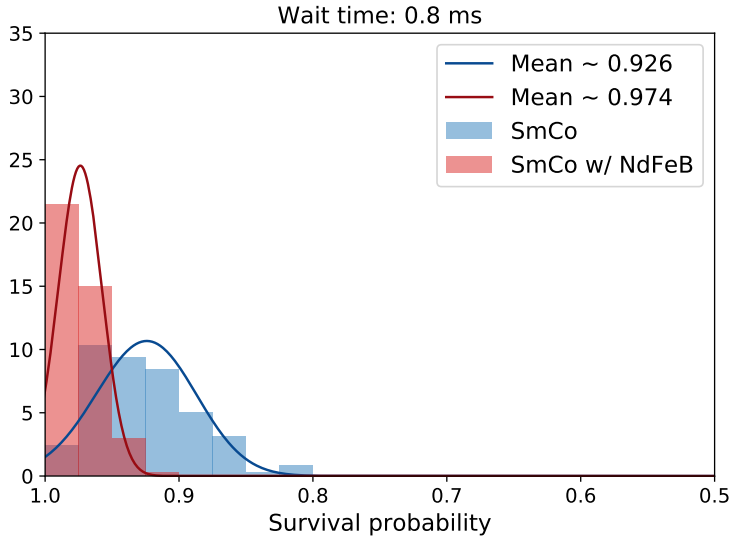

Figure 6.4.: Normed histogram of the survival probability distribution at a wait time of 0.8 ms after every gate. The fit function used here is equation 6.3, corresponding values can be found in table 6.2. The mean average fidelity could be improved from ~ 0.926 with the first permanent magnet setup to ~ 0.974 with the new permanent magnetic system of SmCo compensated with NdFeB.

In table 6.3, the expectation values corresponding to the different error models (details in table 6.1) are calculated based on the fitted σ^2. While the error models both implicate higher expected average mean fidelities, it is not possible from the present measurements to decide which one of the models provides the best prediction. Nevertheless, a great enhancement could be achieved, the average mean fidelity at an idle time of 2.0 ms after each gate could be increased by around 14 % from $\sim$ 72 % to $\sim$ 86 %.

Idle Time (ms)	Magnet Version	α	β	Mean	$\sigma^2 = \alpha\beta^2$
0.4	Old	647	0.0015	0.973	1e-3
0.4	New	24107	4.11e-5	0.99098	4e-5
0.8	Old	612	0.0015	0.926	1e-3
0.8	New	3587	0.0003	0.9740	3e-4
1.4	Old	96	0.0086	0.8256	7e-3
1.4	New	524	0.0018	0.926	2e-3
2.0	Old	31	0.023	0.719	1.6e-2
2.0	New	145	0.0059	0.862	5e-3

Table 6.2.: Fit parameters corresponding to Eq. 6.3 and data represented in Fig. 6.3. All fits confirm, that the new magnetic setup reduces the decoherent effects and therefore the mean fidelity after a certain idle time is increased.

Idle Time (ms)	Magnet Version	Mean	σ^2	$\mathbb{E}$ Markovian	$\mathbb{E}$ DC/Block-correlated
0.4	Old	0.973	1e-3	0.9901	0.9900
0.4	New	0.99098	4e-5	0.9996	0.9996
0.8	Old	0.926	1e-3	0.9901	0.9900
0.8	New	0.9740	3e-4	0.9970	0.9970
1.4	Old	0.8256	7e-3	0.9333	0.9300
1.4	New	0.926	2e-3	0.9803	0.9800
2.0	Old	0.719	1.6e-2	0.8571	0.8400
2.0	New	0.862	5e-3	0.9517	0.9500

Table 6.3.: Fit parameters corresponding to Eq. 6.3 and data represented in Fig. 6.3. The expectation values due to the Markovian and DC/Block-correlated error models are calculated based on the fit $\sigma^2 = \alpha\beta^2$.

Chapter 7

Conclusion and Outlook

In this work, a new software framework is presented, which is able to automatically generate suitable voltage ramps to perform shuttling operations, such as transport over multiple segments and ion crystal separation in a linear segmented Paul trap. The framework has been successfully developed, integrated in the experimental control software and first measurements have been performed. These measurement already show a clear advantage in terms of the shortest shuttling times for multi-segment transport, where excessive motional excitation would impede further quantum logic operations. The next step will be the following:

- To focus on the dynamics, i.e. to finalize the second optimization step, where the voltage ramps are transformed to actual time domain ramps.
- To carry out measurements including the correction for filter-induced distortions, which are expected to show improvements from the automatically generated ramps even more clearly.
- To improve the representation of the trap potentials, in particular to provide options for complementing with spectroscopic calibration data.
- To add the option for inserting ion crystal rotations [Kau17a].
- To apply the framework to complex sequences in a holistic way, i.e. to perform the sequence for four-ion entanglement [Kau17b] entirely based on SITCONS-generated voltage ramps and evaluate the reduction in shuttling overhead.

A further part of this thesis is the design and integration of a new permanent magnet setup for the improvement of the long-time stability of the quantizing field. With a combination of SmCo and NdFeB and a proper alignment devised, to cancel out temperature drift induced magnetic field drifts, we observed a lower dependence of the magnetic field magnitude at the ion location on the temperature drift of around 40 %, compared to the previous design. Additionally, we were able to reduce the temperature drift and in total obtained a tenfold reduction of the qubit frequency drift in a long-time measurement ($> 8\,\mathrm{h}$). Furthermore, we have observed decreased magnetic field drifts on shorter time scales, by carrying out randomized benchmarking measurements on a single qubit, where the error-per-gate induced by off-resonance during idle time between gates was shown to be substantially reduced. Measurements of the

magnetic field along the trap axis have shown an unexpectedly large inhomogeneity. A possible attempt to unify the achieved reduction of the frequency drift and the higher homogeneity could be to combine the advantages of the two designs, the smaller size of the previous magnet frames and the two types of permanent magnets to cancel the temperature induced magnetic field drift.

Appendix A

Appendix

A.1. Further Details on SITCONS Library

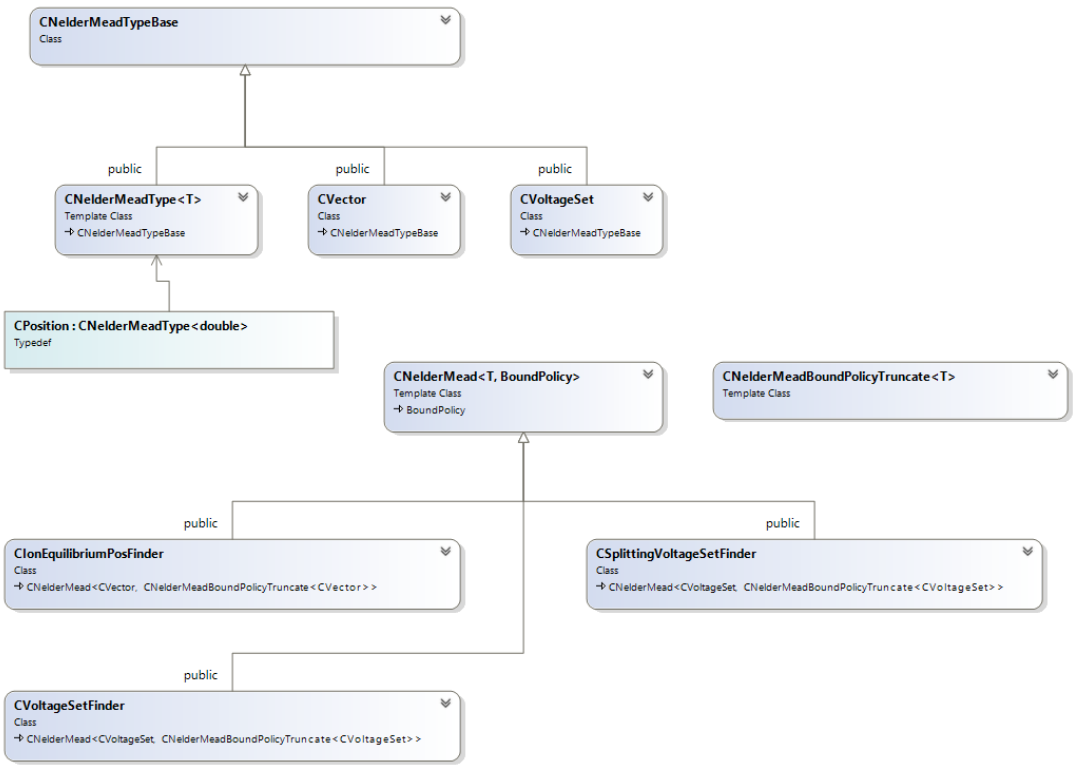

Figure A.1.: Class diagram of the classes closely related to the Nelder Mead optimization.

A.2. Sketch of the New Permanent Magnet Frame

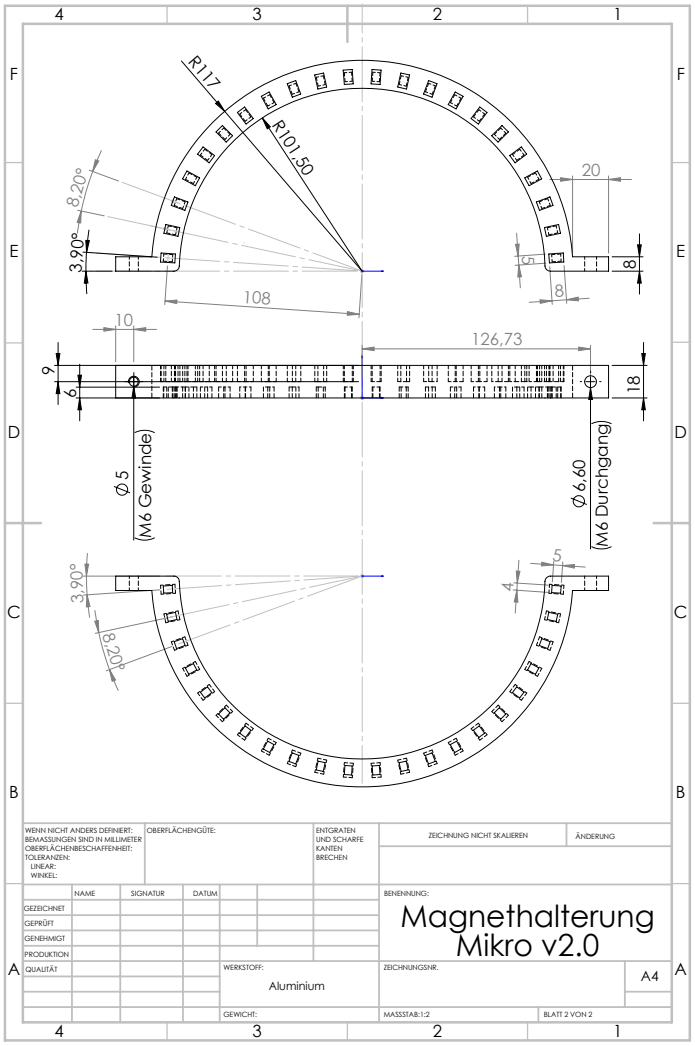

Figure A.2.: Sketch of the magnet frame. Four of this parts are produced to build up the two aluminum rings. The aluminum frames are divided into two parts with each 22 cutouts for Sm_2Co_{17} and 22 cutouts for NdFeB magnets. Dimensions in mm.

List of Figures

List of Tables

Bibliography

[Bal16a] H. Ball, T. M. Stace, S. T. Flammia, and M. J. Biercuk.
Effect of noise correlations on randomized benchmarking.
Phys. Rev. A **93**, 022303, 022303 (2016) .

[Bal16b] C. J. Ballance, T. P. Harty, N. M. Linke, M. A. Sepiol, and D. M. Lucas.
High-Fidelity Quantum Logic Gates Using Trapped-Ion Hyperfine Qubits.
Phys. Rev. Lett. **117**, 060504 (2016) .

[Ben08] J. Benhelm, G. Kirchmair, C. F. Roos, and R. Blatt.
Experimental quantum-information processing with $^{43}Ca^{+}$ *ions*.
Phys. Rev. A **77**, 062306 (2008) .

[Bla01] E. D. Black.
An introduction to Pound–Drever–Hall laser frequency stabilization.
American Journal of Physics **69**, 79–87 (2001) .

[Bla09] R. B. Blakestad, C. Ospelkaus, A. P. VanDevender, J. M. Amini, J. Britton, D. Leibfried, and D. J. Wineland.
High-Fidelity Transport of Trapped-Ion Qubits through an **X***-Junction Trap Array*.
Phys. Rev. Lett. **102**, 153002 (2009) .

[Bol85] J. J. Bollinger, J. D. Prestage, W. M. Itano, and D. J. Wineland.
Laser-Cooled-Atomic Frequency Standard.
Phys. Rev. Lett. **54**, 1000–1003 (1985) .

[Bow12] R. Bowler, J. Gaebler, Y. Lin, T. R. Tan, D. Hanneke, J. D. Jost, J. P. Home, D. Leibfried, and D. J. Wineland.
Coherent Diabatic Ion Transport and Separation in a Multizone Trap Array.
Phys. Rev. Lett. **109**, 080502 (2012) .

[Cho14] J. M. Chow, J. M. Gambetta, E. Magesan, D. W. Abraham, A. W. Cross, B. R. Johnson, N. A. Masluk, C. A. Ryan, J. A. Smolin, S. J. Srinivasan, and M. Steffen.
Implementing a strand of a scalable fault-tolerant quantum computing fabric.
Nature Communications **5** (2014).

[Deb16] S. Debnath, N. M. Linke, C. Figgatt, K. A. Landsman, K. Wright, and C. Monroe.
Demonstration of a small programmable quantum computer with atomic qubits.
Nature **536**, 63–66 (2016).

[Har14] T. P. Harty, D. T. C. Allcock, C. J. Ballance, L. Guidoni, H. A. Janacek, N. M. Linke, D. N. Stacey, and D. M. Lucas.
High-Fidelity Preparation, Gates, Memory, and Readout of a Trapped-Ion Quantum Bit.
Phys. Rev. Lett. **113**, 220501 (2014) .

[Hen06] W. K. Hensinger, S. Olmschenk, D. Stick, D. Hucul, M. Yeo, M. Acton, L. Deslauriers, C. Monroe, and J. Rabchuk.
T-junction ion trap array for two-dimensional ion shuttling, storage, and manipulation.
Applied Physics Letters **88**, 034101 (2006) .

[Hom06] J. P. Home and A. M. Steane.
Electrode Configurations for Fast Separation of Trapped Ions.
Quantum Info. Comput. **6**, 289–325 (2006) .

[Jam98] D. James.

Quantum dynamics of cold trapped ions with application to quantum computation.
Applied Physics B **66**, 181–190 (1998) .

[Kau14] H. Kaufmann, T. Ruster, C. T. Schmiegelow, F. Schmidt-Kaler, and U. G. Poschinger.
Dynamics and control of fast ion crystal splitting in segmented Paul traps.
New Journal of Physics **16**, 073012 (2014) .

[Kau17a] H. Kaufmann, T. Ruster, C. T. Schmiegelow, M. A. Luda, V. Kaushal, J. Schulz, D. von Lindenfels, F. Schmidt-Kaler, and U. G. Poschinger.
Fast ion swapping for quantum-information processing.
Physical Review A: General Physics **95**, 052319, 052319 (2017) .

[Kau17b] H. Kaufmann, T. Ruster, C. T. Schmiegelow, M. A. Luda, V. Kaushal, J. Schulz, D. von Lindenfels, F. Schmidt-Kaler, and U. G. Poschinger.
Scalable creation of long-lived multipartite entanglement.
ArXiv e-prints (2017).

[Kau17c] H. Kaufmann.
A Scalable Quantum Processor.
PhD thesis. Johannes Gutenberg-Universität Mainz, 2017.

[Kel15] J. Kelly, R. Barends, A. G. Fowler, A. Megrant, E. Jeffrey, T. C. White, D. Sank, J. Y. Mutus, B. Campbell, Y. Chen, Z. Chen, B. Chiaro, A. Dunsworth, I.-C. Hoi, C. Neill, P. J. J. O'Malley, C. Quintana, P. Roushan, A. Vainsencher, J. Wenner, A. N. Cleland, and J. M. Martinis.
State preservation by repetitive error detection in a superconducting quantum circuit.
Nature **519**, 66–69 (2015) .

[Kie02] D. Kielpinski, C. Monroe, and D. Wineland.
Architecture for a large-scale ion-trap quantum computer.
Nature **417**, 709–11 (2002).

[Kni08] E. Knill, D. Leibfried, R. Reichle, J. Britton, R. B. Blakestad, J. D. Jost, C. Langer, R. Ozeri, S. Seidelin, and D. J. Wineland.
Randomized benchmarking of quantum gates.
Physical Review A **77**, 012307, 012307 (2008) .

[Lei03] D. Leibfried, R. Blatt, C. Monroe, and D. Wineland.
Quantum dynamics of single trapped ions.
Rev. Mod. Phys. **75**, 281–324 (2003) .

[Mac12] T. Macha.
Frequenzstabilisierung eines Titan-Saphir-Lasers und Verbesserung von Qubits mit Ca+-Ionen.
Diploma Thesis. Johannes Gutenberg-Universität Mainz, 2012.

[Mac14] K. Macieszczak, M. Fraas, and R. Demkowicz-Dobrzański.
Bayesian quantum frequency estimation in presence of collective dephasing.
New Journal of Physics **16**, 113002 (2014) .

[Mon11] T. Monz.
Quantum information processing beyond ten ion-qubits.
PhD thesis. Leopold-Franzens Universität Innsbruck, 2011.

[Mon16] T. Monz, D. Nigg, E. A. Martinez, M. F. Brandl, P. Schindler, R. Rines, S. X. Wang, I. L. Chuang, and R. Blatt.

Realization of a scalable Shor algorithm.
Science **351**, 1068–1070 (2016) .

[Nel65] J. A. Nelder and R. Mead.
A Simplex Method for Function Minimization.
Comput. J. **7**, 308–313 (1965) .

[Nie00] M. A. Nielsen and I. L. Chuang.
Quantum Computation and Quantum Information.
Cambridge University Press, 2000.

[Nig14] D. Nigg, M. Müller, E. A. Martinez, P. Schindler, M. Hennrich, T. Monz, M. A. Martin-Delgado, and R. Blatt.
Quantum computations on a topologically encoded qubit.
Science **345**, 302–305 (2014) .

[Olm07] S. Olmschenk, K. C. Younge, D. L. Moehring, D. N. Matsukevich, P. Maunz, and C. Monroe.
Manipulation and detection of a trapped Yb^+ hyperfine qubit.
Phys. Rev. A **76**, 052314, 052314 (2007) .

[Roo00] C. F. Roos.
Controling the quantum state of trapped ions.
PhD thesis. Universität Ulm, 2000.

[Rus12] T. Ruster.
Schneller Transport von kalten gefangenen Ionen.
Diploma Thesis. Johannes Gutenberg-Universität Mainz, 2012.

[Rus14] T. Ruster, C. Warschburger, H. Kaufmann, C. T. Schmiegelow, A. Walther, M. Hettrich, A. Pfister, V. Kaushal, F. Schmidt-Kaler, and U. G. Poschinger.
Experimental realization of fast ion separation in segmented Paul traps.
Phys. Rev. A **90**, 033410, 033410 (2014) .

[Rus16] T. Ruster, C. T. Schmiegelow, H. Kaufmann, C. Warschburger, F. Schmidt-Kaler, and U. G. Poschinger.
A long-lived Zeeman trapped-ion qubit.
Applied Physics B: Lasers and Optics **122**, 254, 254 (2016) .

[Rus17a] T. Ruster, H. Kaufmann, M. A. Luda, V. Kaushal, C. T. Schmiegelow, F. Schmidt-Kaler, and U. G. Poschinger.
Entanglement-based dc magnetometry with separated ions.
ArXiv e-prints (2017).

[Rus17b] T. Ruster.
Entanglement-enhanced magnetometry with separated trapped ions.
PhD thesis. Universität Mainz, 2017.

[Sch13] P. Schindler, D. Nigg, T. Monz, J. T. Barreiro, E. Martinez, S. X. Wang, S. Quint, M. F. Brandl, V. Nebendahl, C. F. Roos, M. Chwalla, M. Hennrich, and R. Blatt.
A quantum information processor with trapped ions.
New Journal of Physics **15**, 123012 (2013) .

[Shu14] G. Shu, G. Vittorini, A. Buikema, C. S. Nichols, C. Volin, D. Stick, and K. R. Brown.
Heating rates and ion-motion control in a Υ-junction surface-electrode trap.
Phys. Rev. A **89**, 062308 (2014) .

[Sin10] K. Singer, U. Poschinger, M. Murphy, P. Ivanov, F. Ziesel, T. Calarco, and F. Schmidt-Kaler.
Colloquium.
Rev. Mod. Phys. **82**, 2609–2632 (2010) .

[Tim11] N. Timoney, I. Baumgart, M. Johanning, A. F. Varón, M. B. Plenio, A. Retzker, and C. Wunderlich.
Quantum gates and memory using microwave-dressed states.
Nature **476**, 185–188 (2011) .

[Wal12] A. Walther, F. Ziesel, T. Ruster, S. T. Dawkins, K. Ott, M. Hettrich, K. Singer, F. Schmidt-Kaler, and U. Poschinger.
Controlling Fast Transport of Cold Trapped Ions.
Physical Review Letters **109**, 080501, 080501 (2012) .

[Wie16] N. Wiebe and C. Granade.
Efficient Bayesian Phase Estimation.
Phys. Rev. Lett. **117**, 010503 (2016) .

[Win79] D. J. Wineland and W. M. Itano.
Laser cooling of atoms.
Phys. Rev. A **20**, 1521–1540 (1979) .

[Wri13] K. Wright, J. M. Amini, D. L. Faircloth, C. Volin, S. C. Doret, H. Hayden, C.-S. Pai, D. W. Landgren, D. Denison, T. Killian, R. E. Slusher, and A. W. Harter.
Reliable transport through a microfabricated X -junction surface-electrode ion trap.
New Journal of Physics **15**, 033004 (2013) .